Restoring metabolism of microglia by dapsone rescues pathology and improves memory in a mouse model of Alzheimer's disease

Shufei Feng,[1†] Nianzhuang Qiu,[2†] Tangsheng Lu,[2] Lei Han,[2] Zihang Li,[3] Siyu Liu,[1] Liyuan Guo,[3] Chunxia Huang,[3] Lu Cao,[1] Xiaoxing Liu,[1] Jie Shi,[2] Qingqing Yin,[4, *] Furen Zhang,[5, *] Ya Bin Wei,[2, *] Lin Lu,[1, 3, 6, *] Kai Yuan[1, *]

1. Peking University Sixth Hospital, Peking University Institute of Mental Health, NHC Key Laboratory of Mental Health (Peking University), National Clinical Research Center for Mental Disorders (Peking University Sixth Hospital), Beijing, China.
2. National Institute on Drug Dependence and Beijing Key Laboratory of Drug Dependence Research, Peking University, Beijing, China.
3. Shandong Institute of Brain Science and Brain-inspired Research; Medical Science and Technology Innovation Center, Shandong First Medical University & Shandong Academy of Medical Sciences, Jinan, Shandong Province, China
4. Department of Geriatric Neurology, Shandong Provincial Hospital Affiliated to Shandong First Medical University, Jinan, Shandong, China.
5. Hospital for Skin Diseases, Shandong First Medical University, Jinan, Shandong, China.
6. Peking-Tsinghua Center for Life Sciences and PKU-IDG/McGovern Institute for Brain Research, Peking University, Beijing, China.

† These authors contributed equally to this work.

* **Correspondence:**
Prof. Kai Yuan, PhD, Institute of Mental Health and Peking University Sixth Hospital, 51 Huayuanbei Road, Beijing, 100191, China.
E-mail: yuankai@pku.edu.cn

Prof. Lin Lu, MD, PhD, Institute of Mental Health and Peking University Sixth Hospital, 51 Huayuanbei Road, Beijing, 100191, China.
E-mail: linlu@bjmu.edu.cn

Prof. Yabin Wei, PhD, National Institute on Drug Dependence and Beijing Key Laboratory of Drug Dependence Research, Peking University, Beijing, 100191, China
E-mail: yabin.wei@bjmu.edu.cn

Prof. Furen Zhang, PhD, Hospital for Skin Diseases, Shandong First Medical University, Jinan, Shandong, 250021, China.
Email: zhangfuren@hotmail.com

Prof. Qingqing Yin, PhD, Department of Geriatric Neurology, Shandong Provincial Hospital Affiliated to Shandong First Medical University, Jinan,

1 Shandong, 250021, China.
2 Email: yinqingqing@sdfmu.edu.cn

Abstract

Background

Alzheimer's disease (AD) is characterized by progressive cognitive decline and neuropathological changes, with increasing evidence implicating dysregulated microglial immunometabolism. Dapsone (DDS), a clinically approved anti-leprosy drug with reported anti-inflammatory and neuroprotective properties, has not been evaluated for its capacity to regulate microglial metabolism in AD.

Methods

The therapeutic effects and potential mechanisms of DDS were examined in triple-transgenic AD mice (3×Tg-AD mice) and amyloid-β oligomer (oAβ)-challenged microglial models. Following six weeks of oral DDS treatment, cognitive performance, AD-related pathology, hippocampal synaptic plasticity, and microglial morphology and function were assessed using behavioral, histological, biochemical, and electrophysiological analyses. Microglial metabolic and transcriptional states were assessed using extracellular flux analysis and single-cell RNA sequencing (scRNA-seq), and cerebral glucose utilization was evaluated by FDG-PET. Chemical proteomics was used to identify potential DDS-interacting proteins. Microglia-specific PRAS40 overexpression and knockdown were performed to assess the functional relevance of PRAS40. Statistical analyses used appropriate parametric or non-parametric tests.

Results

DDS improved hippocampus dependent cognitive performance, reduced Aβ deposition and tau phosphorylation, and restored impaired hippocampal synaptic plasticity in 3×Tg-AD mice. DDS remodeled microglial morphology toward a homeostatic-like phenotype and enhanced the phagocytic uptake of Aβ and synaptosomes in oAβ-challenged microglia. scRNA-seq revealed DDS associated changes in microglial transcriptional states, characterized by enrichment of homeostatic and proteostasis-related gene programs and attenuation of inflammatory microglial signatures. DDS restored microglial mitochondrial function and shifted microglial metabolism from glycolysis toward mitochondrial respiration. Proline-rich Akt substrate of 40 kDa (PRAS40) was identified as a DDS-interacting protein, and DDS suppressed PRAS40–mTORC1 signaling. Consistently, DDS partially normalized hippocampal glycolytic and tricarboxylic acid cycle metabolism and improved cerebral glucose utilization in 3×Tg-AD mice. Microglia-specific PRAS40 overexpression attenuated the cognitive and pathological effects of DDS, whereas PRAS40 knockdown produced effects like those of DDS.

Conclusions

DDS alleviated cognitive deficits and AD-related pathology in 3×Tg-AD mice, accompanied by improved microglial mitochondrial function, altered microglial transcriptional states, and reduced PRAS40–mTORC1 signaling. Microglial

PRAS40–mTORC1 signaling may contribute to the effects of DDS by regulating microglial metabolism. Targeting this pathway may provide a potential therapeutic strategy for AD.

Keywords

Alzheimer's disease, Immunometabolism, Microglia, Dapsone, PRAS40

Introduction

Alzheimer's disease (AD) is a progressive neurodegenerative disorder and a leading cause of dementia, and no effective curative therapy is currently available. Despite decades of research, many earlier trials targeting amyloid-β (Aβ) and tau pathology have shown limited clinical benefit, with adverse effects

restricting the use of some candidates [1-5]. Recent anti-Aβ immunotherapies have shown promise in slowing disease progression, but their long-term safety, accessibility, and cost-effectiveness remain unresolved challenges [6-9]. These challenges indicate that targeting protein aggregation alone may be insufficient, supporting the need to better understand how immune processes contribute to neurodegeneration.

Microglia, the resident immune cells of the brain, play a central role in AD pathogenesis [10-14]. In addition to mediating neuroinflammatory responses, microglia regulate synaptic pruning, Aβ clearance, phagocytosis, and lysosomal degradation. These functions are closely linked to the metabolic state of microglia. In response to Aβ accumulation and tau pathology, microglia undergo metabolic reprogramming marked by a shift from mitochondrial oxidative phosphorylation (OXPHOS) toward glycolysis [15-18]. This metabolic shift impairs mitochondrial energy metabolism and lysosomal degradation, leading to defective Aβ clearance, impaired microglial homeostasis, and sustained neuroinflammation [19, 20]. Thus, targeting microglial metabolism may help restore microglial homeostasis in AD.

Dapsone (4,4′-diaminodiphenyl sulfone, DDS) is a long-used first-line drug for leprosy, with a well-documented safety profile [21-25]. Beyond its antimicrobial activity, DDS has been shown to modulate inflammatory signaling in both peripheral immune cells and the central nervous system [26, 27].

Epidemiological studies have reported a lower incidence of dementia among patients receiving long-term DDS treatment for conditions other than AD, although causality has not been established [28, 29]. Whether DDS affects microglial function and AD pathology remains unclear.

In this study, we examined the effects of DDS in a triple-transgenic AD (3×Tg-AD) mouse model. We found that DDS improved cognitive performance, reduced Aβ accumulation, and increased microglial phagocytosis. We then focused on microglial metabolism and examined how DDS affects mitochondrial OXPHOS, mechanistic target of rapamycin complex 1 (mTORC1) signaling, and autophagic activity. We further identified PRAS40 as a key regulator involved in DDS-mediated restoration of microglial function. These findings suggest that impaired microglial metabolism contributes to AD pathology and that restoring microglial metabolic function may help improve AD related outcomes.

Methods

Animals

The 3×Tg-AD mice was generated at the University of California, Irvine by introducing APPSwe and tauP301L transgenes into a presenilin 1 with the M146V mutation knock-in single-cell embryo on a C57BL6/129SvJ hybrid background [30, 31]. 3×Tg-AD and C57BL/6 male mice (wild-type; 20-25 g; 8-

10 weeks) were obtained from Wuhan Wukong Laboratory Animal Co. Ltd (Hubei, China). Mice were housed 4-5 per cage under a 12-h light/dark cycle with ad libitum access to food and water. Animals were randomly assigned to treatment groups, and all outcome assessments were performed under blinded conditions. All procedures were approved by the Animal Care Committee of Peking University.

Drug administration

Dapsone (DDS, 4,4'-diaminodiphenyl sulfone; Sigma-Aldrich, 46158, Darmstadt, Germany) was dissolved in DMSO and diluted in corn oil to the desired concentration. In the absence of prior DDS studies in AD mouse models, dosing was guided by relevant experimental evidence [32, 33]. Safety in 3×Tg-AD mice was evaluated by behavioral monitoring and body weight. A dose of 10 mg/kg was selected as the optimal therapeutic regimen for subsequent experiments.

Behavioral assessment

Treatment was initiated at 10 months and continued for 6 weeks. Behavioral testing, including open field test, novel object recognition test, T-maze test, and Morris water maze test, was conducted at 11.5 months of age after 6 weeks of treatment.

Open field test

Exploration and anxiety-like behavior were assessed in a 50 × 50 cm^2 open field. Mice were dark-adapted for 30 min, placed in the arena, and allowed 1 min of habituation, followed by a 10-min recording using Anymaze (Noldus). Total distance traveled and time spent in center versus peripheral zones were quantified.

Novel object recognition

Mice were placed in an open field containing two identical objects (sample session, 10 min). 24 h later, one object was replaced with a novel object of similar size and texture but different shape (test session, 10 min). Exploration was defined as the nose oriented toward the object within 2 cm. Time and number of explorations for each object were recorded, and the discrimination performance was calculated.

Spontaneous alternation T-maze test

Spatial working memory was assessed using a spontaneous alternation T-maze task [34]. Mice were acclimated to the testing room for 1 h before being placed in the central zone of the maze and allowed to explore. Arm entries were recorded using a ceiling-mounted HD camera. An arm entry was defined as all four paws entering an arm. Across six consecutive trials, re-entry into the previously visited arm was scored as an error, whereas entry into the alternate

arm was scored as a correct alternation. The alternation percentage was calculated as (number of correct alternations / 6) × 100.

Morris water maze

Spatial learning and memory were assessed using the Morris water maze (MWM) paradigm as previously described [35]. The apparatus consisted of a circular pool filled with opaque water maintained at 26℃with a depth of 16 cm. A hidden platform was submerged 1 cm below the surface in a fixed quadrant. Mice received two training trials per day for 5 days; if the platform was not located within 60 s, mice were guided to it and kept there for 10 s. Escape latency was recorded using Ethovision (Noldus). On day 6, the platform was removed and a 60-s probe trial was performed to measure swimming trajectory and time spent in each quadrant.

Tissue dissociation and preparation of single-cell suspensions

Fresh tissues were transferred into pre-chilled RNase-free 1× PBS (Ca^{2+}/Mg^{2+}-free), rinsed, minced into ~0.5 mm^2 pieces, and digested in a solution containing 0.35% collagenase IV, 2 mg/mL papain, and 120 U/mL DNase I at 37℃ for 20 min (100 rpm). Digestion was stopped with PBS containing 10% fetal bovine serum (FBS). Cell suspensions were gently triturated, filtered through 70-30 μm strainers, and centrifuged at 300 × g for 5 min at 4℃. Pellets were resuspended in 1× PBS with 0.04% BSA, erythrocytes were lysed with 1×

lysis buffer for 2-10 min, and dead cells were removed using Dead Cell Removal MicroBeads and MS Columns (Miltenyi Biotec; MACS 130-090-101, 130-042-201). After two washes (300 × g, 5 min, 4℃), viability (>85%) was confirmed by trypan blue, and cells were adjusted to 700-1200 cells/μL for downstream processing.

Chromium 10x Genomics library preparation and sequencing

Single-cell suspensions were loaded onto Chromium chips using the 10x Genomics Chromium Single Cell 3′ Kit v3, targeting 8,000 cells per sample. cDNA amplification and library construction were performed according to the manufacturer's protocol. Libraries were sequenced on an Illumina NovaSeq 6000 platform with paired-end 150-bp reads by LC-Bio Technology (Hangzhou, China), with a minimum sequencing depth of 20,000 reads per cell.

Bioinformatics analysis

Sequencing data were processed using Cell Ranger v7.0.0 for read alignment, cell calling, and transcript quantification. Gene expression matrices were imported into Seurat v4.1.0 for quality control, normalization, dimensional reduction, clustering, and UMAP visualization. Cells with fewer than 500 detected genes or more than 25% mitochondrial gene expression were excluded. Gene expression was normalized using the LogNormalize function in Seurat. Principal component analysis was performed, and the top 20 principal

components were used for clustering and UMAP visualization. Marker genes for each cluster were identified using FindAllMarkers with the following criteria: expression in at least 10% of cells within a cluster, adjusted p value ≤ 0.01, and log fold change ≥ 0.26. Cell types were annotated using SingleR, scCATCH, and LC-Marker, together with canonical marker genes. KEGG pathway enrichment analysis was performed on differentially expressed genes to identify enriched functional pathways. Microglial dynamics were further examined using Monocle 2-based pseudotime trajectory analysis and CellChat-based ligand-receptor interaction analysis. Cluster annotations were further refined to characterize distinct microglial states.

Microglial sub-clustering and state annotation

Microglial states were annotated based on cluster-enriched marker genes and published microglial signatures, including homeostatic microglia (HM), disease associated microglia (DAM), microglial neurodegenerative phenotype (MGnD), and cycling/proliferating microglia (CPM). Based on the enriched expression of these marker genes, microglial clusters were grouped into six annotated states: HM-P2ry12, HM-mt_Nd2, DAM1-Nfkbia, DAM1-CPE, DAM2, and CPM.

HM-P2ry12 was defined by enriched expression of homeostatic markers, including *P2ry12*, *Cx3cr1*, and *Olfml3*. *HM-mt_Nd2* was defined by enriched expression of mitochondrial genes, including *mt-Cytb*, *mt-Nd1*, and *mt-Nd2*.

DAM1-*Nfkbia* was defined by enriched expression of inflammatory and early DAM markers, including *Nfkbia*, *Nfkbiz*, and *Atf3*. DAM1-CPE was defined by enriched expression of *Aldoc*, *Clu*, and *Cpe*, together with retained expression of homeostatic microglial markers. DAM2 was defined by enriched expression of DAM/MGnD markers, including *Apoe*, *Clec7a*, *Cst7*, *Lpl*, *Ccl6*, and *Spp1*. CPM was defined by enriched expression of cell-cycle markers, including *Mki67* and *Top2a*. Because HM-mt_Nd2 represented a small cluster with mitochondrial gene enrichment, it was retained after quality control and included in the annotation, but it was not used as a major basis for downstream mechanistic interpretation.

In situ sequencing

To spatially validate scRNA-seq–defined microglial transcriptional changes, in situ sequencing (ISS) was performed on whole-brain coronal cryosections from 3×Tg mice. Fresh-frozen brains were sectioned at 10 μm thickness, and gene-specific paired probes were used to detect target transcripts. UBC and PPIB served as positive controls and dapB as a negative control; sections were considered qualified if UBC and PPIB were robustly detected and dapB showed minimal background. Following fixation, dehydration, and permeabilization, paired probes hybridized to adjacent mRNA regions and were ligated to form circular DNA templates, which were amplified by rolling-circle amplification.

Cyclic fluorescence imaging was performed to read barcode sequences in situ, with DAPI counterstaining. Images from different sequencing cycles were aligned using feature-based registration, followed by spot detection, barcode decoding, and assignment of transcripts to cells after DAPI-based cell segmentation using Cellpose. For each mouse, one whole-brain section was analyzed, and a single hippocampal CA1 region of interest (ROI) was selected. Microglia were defined as *P2ry12*-positive cells, and *PRAS40* and *Cpe* transcript counts were quantified per microglial cell within the CA1 ROI. Quantification was performed at the mouse level (n = 3 mice per group), with data presented as mean ± SD. Statistical significance between groups was assessed using two-tailed unpaired t-tests.

Cell culture and reagents

BV2 microglia were a kind gift from Prof. Wei. Cells were cultured in high-glucose DMEM supplemented with 10% FBS and 1% penicillin/streptomycin and maintained at 37℃ in a humidified 5% CO_2 atmosphere unless otherwise stated.

Primary microglia culture

Primary mouse microglia were isolated from 0- to 4-day-old neonatal mouse brains as described previously [36]. Brains were dissected and digested with 0.125% trypsin. Cells were plated in poly-D-lysine–coated flasks in DMEM/F12

with 10% heat-inactivated FBS and 1% penicillin/streptomycin and maintained at 37℃ in 5% CO_2. After 24 h, medium was replaced, and cultures were maintained for an additional 2-4 days. Cells were then centrifuged at 400 × g for 10 min, and microglia were resuspended and plated for assays.

Cell Counting Kit-8 (CCK-8) assay

BV2 cells were seeded in 96-well plates at 5 × 10^3 cells/well and treated with DDS (0, 12.5, 25, 50, 100, 200 μg/mL) for 24 or 48 h. CCK-8 solution (10 μL; Beyotime, S0026, Shanghai, China) was added for 4 h, and absorbance at 450 nm was measured. Cell viability (%) was calculated as: [(A_{450} treatment − A_{450} blank)/(A_{450} control − A_{450} blank)] × 100.

Phagocytosis assays

BV2 cells were treated with or without DDS (100 μg/mL) for 24 h. For pHrodo Red-labeled synaptosome uptake, mice were perfused with PBS, brains were homogenized in Syn-PER (Thermo Fisher Scientific, Dreieich, Germany), and synaptosomes were isolated by centrifugation at 15,000 × g. Synaptosomes were labeled with pHrodo iFL Red Microscale Protein Labeling Kit (Thermo Fisher), applied to BV2 cells, and uptake was quantified after fixation with 4% paraformaldehyde by imaging three random fields per well. For fluorescent -labeled Aβ peptide (fAβ(1-42), labeled by HiLyte™ Fluor 555, AnaSpec, AS-60480-01, Fremont, CA, USA) phagocytosis, cells were incubated with 5 μM.

Measurement of ROS, mitochondrial membrane potential, and ATP

Microglia were seeded in 96-well plates and allowed to adhere for 24 h, followed by treatment with DDS (100 μg/mL) for 24 h and subsequent exposure to oAβ (1.0 μM) for an additional 24 h. Mitochondrial reactive oxygen species (ROS) were measured using MitoSOX™ Red (Thermo Fisher Scientific, M36008) at a final concentration of 2 μM for 10 min at 37 ℃ in the dark. After PBS washes, cells were maintained in phenol red–free DMEM and imaged using an inverted confocal microscope. Quantification was performed at the single-cell level, with cells randomly sampled from three independent wells per condition (50 cells per group). Mitochondrial membrane potential was assessed using tetramethylrhodamine ethyl ester (TMRE) (Thermo Fisher Scientific, T669) at 50 nM for 30 min at 37 ℃, followed by PBS washes and confocal imaging. Single-cell fluorescence intensity was quantified from three independent wells, with a total of 75 cells analyzed per group. ATP levels were measured using a luminescent ATP assay kit (Beyotime, S0026) according to the manufacturer's instructions. Cells were lysed in 200 μL of lysis buffer, sonicated, and centrifuged at 12,000 × g for 5 min at 4℃. ATP content was normalized to protein concentration determined by a BCA assay (562 nm; Bio-Rad Multiscan MK3) and expressed relative to control. n = 3 independent experiments per group.

Protein extraction

Briefly, mice were euthanized, and hippocampi were rapidly dissected and frozen on dry ice. Tissue was homogenized in T-PER buffer (Thermo Fisher, 78510) supplemented with protease and phosphatase inhibitors. Homogenates were centrifuged at 100,000 × g for 30 min at 4℃, and supernatants were stored at −80℃ for Western blot.

Western blot

Total hippocampal protein was quantified with a Pierce BCA assay (Thermo Fisher, 23225), separated by SDS-PAGE, and transferred to PVDF membranes (Millipore, IPFL00005, Burlington, MA, USA). Membranes were blocked with 5% skim milk, incubated with primary antibodies overnight at 4℃, and then with HRP-conjugated secondary antibodies for 2 h at room temperature. Signals were developed using Immobilon Western Chemiluminescent HRP Substrate (Sigma-Aldrich, WBKLS0500). Samples from all groups were run in parallel and normalized to internal controls. Normalized values from independent experiments were pooled for statistical analysis.

Immunohistochemistry

Mice were anesthetized with 3% isoflurane and perfused with 0.9% saline. Brains were post-fixed in 4% paraformaldehyde at 4℃ for 24 h, cryoprotected in 5-20% sucrose at 4℃ for 48 h, and frozen in precooled isopentane. Coronal

sections (40 μm) were cut on a cryostat and stored free-floating in 1× PBS with 0.05% sodium azide. Regions of interest were delineated on DAPI counterstaining using ImageJ, and mean gray values and percentage of immunopositive pixels were quantified using a fixed threshold. High-magnification (60×) confocal images of hippocampal microglia were imported into ImageJ (Bio-Formats), reconstructed in 3D with the SNT plugin, and analyzed for branching parameters and Sholl profiles. For Sholl analysis, concentric circles at 10 μm intervals were drawn from the soma center, and intersections and maximum radius were quantified.

Thioflavin S staining

Free-floating sections were washed in PBS, incubated with 500 μM Thioflavin S (Sigma-Aldrich, T1892) in 50% ethanol for 8 min at room temperature, rinsed twice in 50% ethanol, and washed in PBS. Sections were coverslipped and imaged at 20× magnification with a TissueFAXS plus system (TissueGnostics, Vienna, Austria). Amyloid plaque number and area were quantified using ImageJ.

Metabolomic profiling and analysis

Targeted metabolomics of bilateral hippocampi was performed using the Q300™ Metabolite Array (Metabo-Profile Biotechnology, Shanghai, China). Samples were analyzed on an ACQUITY UPLC–Xevo TQ-S system (Waters

Corp). Metabolites were identified using the Metabo-Profile LIMS system, and raw data were processed with TMBQ software for integration, calibration, and quantification. Relative abundances were $\log_2$-transformed, Z-scores were calculated, and heatmaps were generated using the Complex Heatmap package in R.

Electrophysiology

Electrophysiological recordings were performed as described (37). Brains from 12-month-old mice (treated with or without DDS) were rapidly removed into ice-cold oxygenated dissection buffer. Coronal hippocampal slices (350 μm) were prepared with a vibratome (Leica, VT1200S, Wetzlar, Germany) and incubated in ACSF at 30℃ for 20 min and then at room temperature for 40 min. Slices were transferred to a recording chamber perfused with ACSF (1 mL/min). EPSPs were recorded in CA1 using glass pipettes (4-7 MΩ) under a ×40 water immersion lens with DIC optics and a CCD camera. A concentric bipolar electrode delivered stimulation, and LTP was induced by theta-burst stimulation after a 20-min baseline.

Measurement of real-time ECAR and OCR

ECAR and OCR were measured using the Seahorse XF Glycolysis Stress Test Kit (Agilent Technologies, 103020-100, Santa Clara, CA, USA) and Cell Mito Stress Test Kit (Agilent, 103015-100), respectively. BV2 cells (2×10^5) or

primary microglia (1×10^5) were plated in XFe96 microplates and incubated overnight. Sensor cartridges were hydrated overnight at 37℃ in a CO_2-free incubator. Before assays, water was replaced with XF calibrant (pH 7.4) for 1 h. Baseline ECAR/OCR was recorded, followed by sequential injections of glucose, oligomycin, and 2-deoxyglucose (for ECAR) or oligomycin, FCCP, and rotenone/antimycin A (for OCR). Assays were performed in Seahorse XF DMEM (pH 7.4), and data were analyzed with Wave software (Agilent).

Drug Affinity Responsive Target Stability (DARTS)

DARTS was used to assess protein-small molecule interactions. Cell lysates (100 μg protein) were incubated at 25℃ for 10 min with or without the test compound. Proteinase K (Sigma-Aldrich, P2308) was added at a 1:100 enzyme/substrate ratio and incubated at 25℃ for 5 min. Samples were resolved by SDS-PAGE, and protected protein fragments were analyzed by LC-MS and molecular docking to identify candidate targets and binding sites.

Molecular docking and virtual screening

The PRAS40 structure (AF-Q96B36-F1) was obtained from AlphaFold/UniProt and prepared in Schrödinger Maestro using the Protein Preparation Wizard (water removal, missing side-chain rebuilding, hydrogen addition, and energy minimization with OPLS2005 or OPLS3e). Receptor grids were generated around Arg70, Ala45, Pro41, and His63 (site 1) with a 20 $Å^3$ box. Binding

pockets were also evaluated with SiteMap, and the top-ranked site (SiteMap_1_site_1) was used when applicable. The SPECS compound library (https://specs.net/) was processed with LigPrep, generating up to five conformers per ligand with Epik protonation states at pH 7.0 ± 2.0. Virtual screening was performed using Glide in a high-throughput (HTVS), standard precision (SP), and extra precision (XP) workflow. The top 10% of HTVS hits were subjected to SP docking, and the top 5% of SP hits to XP docking. XP scores were used to rank compounds by predicted affinity, and representative poses were visualized with PyMOL.

Surface plasmon resonance

SPR binding assays were performed on a Biacore T200 (Cytiva). Recombinant PRAS40 was immobilized on a CM5 sensor chip. Compounds were injected in PBS with 5% DMSO (20 mM Tris-HCl, 5 mM $MgCl_2$, 150 mM NaCl, pH 7.4) at 30 μL/min with a 60-s association and 150-s dissociation phase. Concentration series (0.78-200 μM) were tested. An unmodified flow cell served as reference. Sensorgrams were processed with Biacore T200 Control Software v3.0, and specific responses were obtained by reference subtraction.

FDG-PET analysis of brain glucose metabolism

Brain glucose metabolism was evaluated using a micro-PET/CT scanner (Super Nova PET/CT, PINGSENG, Shanghai, China). Mice were fasted

overnight and scanned 1 h after DDS administration. Mice were warmed at 37℃ for 30 min, injected intraperitoneally with ^{18}F-FDG (160 MBq/kg, <0.2 mL), allowed a 50-min uptake period, and then anesthetized and positioned in a dedicated imaging bed. PET images were reconstructed and co-registered with CT using MIA software (PINGSENG). Standardized uptake values (SUVs), normalized to injected dose and body weight, were calculated for automatically segmented brain regions.

Viral microinjection

Adeno associated viral (AAV) vectors were generated by Brain Case Technology (Wuhan, China). For microglia-specific PRAS40 overexpression, an AAV vector expressing mouse PRAS40 under the control of the mIBA1 promoter was used (rAAV-mIBA1-PRAS40-P2A-EGFP-WPRE-4×miR9T; hereafter referred to as rAAV-PRAS40). The corresponding control virus expressed EGFP alone under the same promoter (rAAV-mIBA1-EGFP-WPRE-4×miR9T; referred to as rAAV-C.V.). For microglia-specific PRAS40 knockdown, an miR30a-based short hairpin RNA (shRNA) targeting mouse PRAS40 was packaged into rAAV (rAAV-mIBA1-EGFP-5′miR30a-shRNA (mPRAS40)-3′miR30a-WPRE-4×miR9T; referred to as rAAV-shPRAS40). A matched scramble shRNA virus was used as control (rAAV-mIBA1-EGFP-5′miR30a-shRNA (Scramble)-3′miR30a-WPRE-4×miR9T; referred to as rAAV-shC.V.). All viral preparations had titers >1.0 × 10^{13} vg/mL. Male 3×Tg-AD mice

(35-36 weeks of age) were anesthetized with 1.8-2% isoflurane and bilaterally injected into the hippocampal CA1 region (0.5 μL per side) at the following stereotaxic coordinates relative to bregma: −2.0 mm anteroposterior, +1.5 mm mediolateral, and −1.7 mm dorsoventral. After injection, mice were maintained on a heating pad until full recovery and then housed for 6 weeks to allow stable viral expression in parallel with DDS or vehicle treatment before behavioral testing and tissue collection.

Statistical analysis

All experiments used randomized group allocation and blinded outcome assessment. Statistical analyses were performed in GraphPad Prism 10 (GraphPad Software). Two-group comparisons used Student's t-test; multiple group comparisons used one-way ANOVA followed by Tukey's post hoc test. Statistical significance was defined as $p < 0.05$. All data points were included unless excluded based on predefined outlier criteria and reported accordingly.

Results

DDS attenuates hippocampus-dependent cognitive deficits in 3×Tg-AD mice

To assess the effects of DDS in AD, we used 3×Tg-AD mice, which recapitulate key pathological and metabolic features of the disease [31, 37]. We administered oral DDS to 10- to 12-month-old 3×Tg-AD mice (**Figure 1A**). In

the open-field test, 3×Tg-AD mice spent significantly less time in the center compared to control mice. DDS treatment significantly increased center exploration, indicating reduced anxiety-like behavior, without affecting travel velocity or total distance, suggesting preserved motor function (**Figure 1B**).

Hippocampus-dependent cognitive performance was next evaluated using the novel object recognition (NOR), T-maze, and Morris water maze (MWM) tests. In the NOR test, 3×Tg-CON mice exhibited a significantly reduced discrimination index compared with C57-CON and C57-DDS mice, whereas 3×Tg-DDS mice showed a marked increase relative to 3×Tg-CON mice, indicating that DDS improved object recognition performance (**Figure 1C**). In the T-maze test, spontaneous alternation performance was substantially lower in 3×Tg-CON mice than in C57-CON and C57-DDS mice, while 3×Tg-DDS mice displayed significantly enhanced alternation behavior compared with 3×Tg-CON mice, reflecting improved cognitive flexibility and spatial working memory (**Figure 1D**). In the MWM test, 3×Tg-CON mice showed pronounced impairments in spatial learning and memory relative to both C57 groups, as evidenced by fewer platform crossings and reduced time spent in the target quadrant. These deficits were significantly alleviated in 3×Tg-DDS mice (**Figure 1E**). DDS administration did not alter cognitive performance in C57 mice across any behavioral paradigm. Together, these results demonstrate that DDS alleviates hippocampus-dependent learning and memory deficits in AD mice

without affecting baseline behavior in wild-type animals.

To further assess tolerability, a 6-week dose-escalation study (0, 5, 10, and 50 mg/kg) was conducted in 3×Tg-AD mice. DDS administration had no significant effect on body weight across all doses tested, including doses fivefold higher than the experimental regimen (**Figure S1**).

DDS attenuates hippocampal pathology and modulates synaptic plasticity in 3×Tg-AD mice

Given the central role of the hippocampus and Aβ pathology in learning and memory deficits in AD [38], we next examined whether DDS associated cognitive improvements were accompanied by changes in hippocampal Aβ deposition and synaptic pathology. Thioflavin S staining revealed that DDS treatment significantly reduced dense-core plaque burden in the hippocampal CA1 region, whereas a similar trend toward reduced plaque load was observed in the dentate gyrus (DG) (**Figure 1F, Figure S2A-B**). Consistently, immunofluorescence analysis using the 6E10 antibody demonstrated a robust reduction of Aβ plaque burden in CA1 following DDS treatment, while DG exhibited a directionally consistent but statistically non-significant decrease in Aβ immunoreactivity (**Figure S2C-F**). Moreover, electrophysiological recordings revealed that DDS treatment enhanced hippocampal long-term

potentiation (LTP), with increased field excitatory postsynaptic potential (fEPSP) amplitude, indicating restored synaptic plasticity (**Figure 1G**). Western blot analysis confirmed that DDS treatment significantly reduced hippocampal Aβ expression, tau phosphorylation at Ser202/Thr205 (AT8) and Thr231 (AT180) epitopes, as well as total tau levels (HT7) (**Figure 1H-I**). Together, these results demonstrate that DDS reduces hippocampal pathology and restores synaptic function, which likely contributes to the cognitive improvements observed in 3×Tg-AD mice.

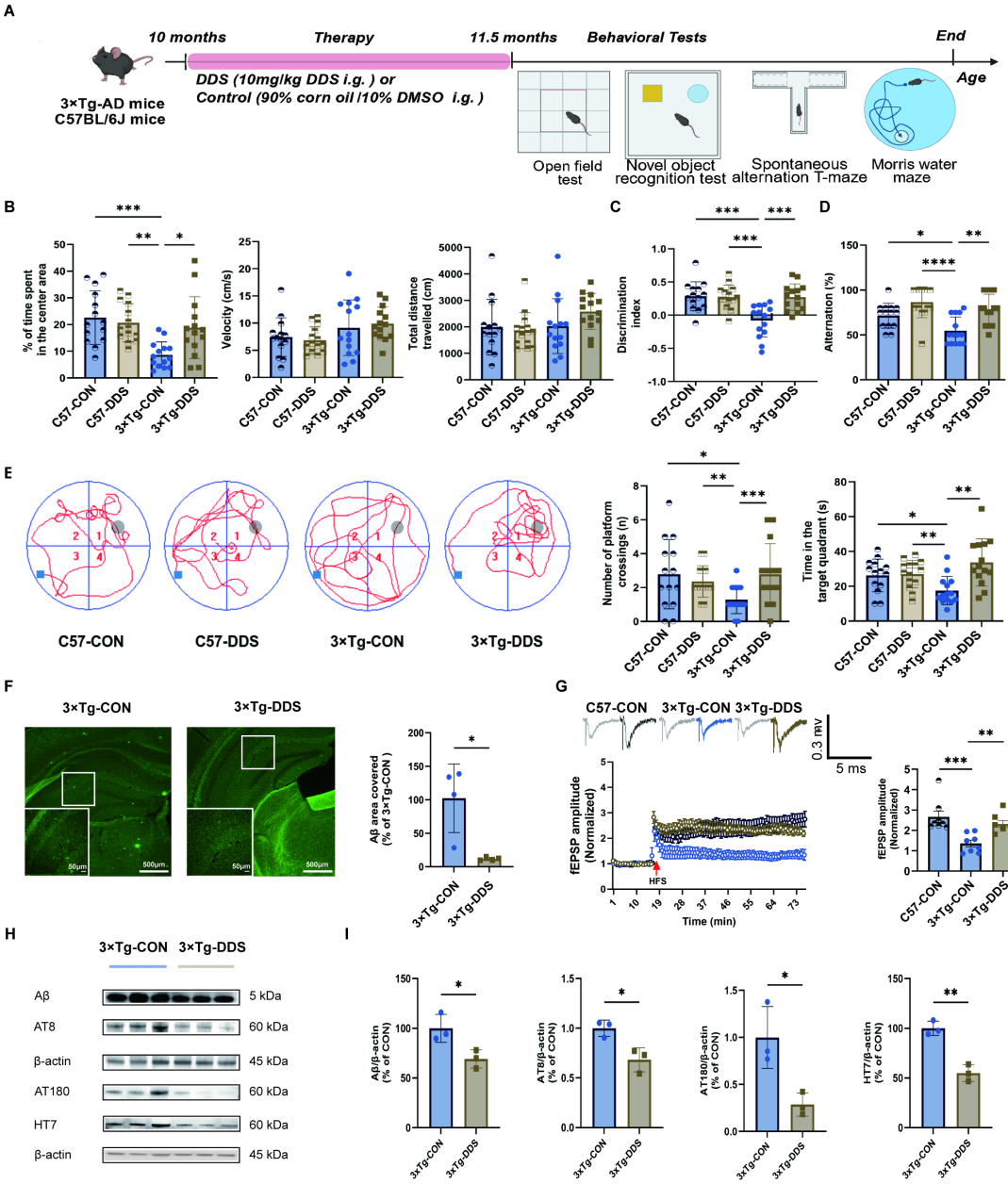

Figure 1. DDS treatment restores cognitive function and attenuates hippocampal AD pathology in 3×Tg-AD mice.

(A) Experimental timeline of DDS administration for C57BL/6J and 3×Tg-AD mice (n = 14 mice per group).

(B–D) Behavioral assessments, including open field test parameters-time spent in the center, velocity, and total distance (B), the discrimination index in the NOR test (C), and spontaneous alternation in the T-maze (D).

(E) Morris water maze performance showing representative probe-trial swimming paths (left), number of platform entries (middle), and time spent in the target quadrant (right).

(F) Thioflavin S staining of hippocampal Aβ plaques in 3×Tg-CON and 3×Tg-DDS mice, with magnified CA1 views and quantification of ThS-positive plaque area (n = 4 mice per group). Scale bars: 500 μm (hippocampus), 50 μm (CA1).

(G) Long-term potentiation in CA1, showing normalized fEPSP responses after high-frequency stimulation in C57 control and 3×Tg-AD mice ± DDS (n = 8 slices from 3 mice per group), with bar graph representing mean fEPSP during the final 5 min.
(H–I) Western blot analysis of hippocampal AD related proteins in 3×Tg-CON and 3×Tg-DDS mice, including representative immunoblots and densitometric quantification of Aβ, phospho-tau (AT8, AT180), and total tau (HT7), normalized to β-actin (n = 3 per group).
Data are presented as mean ± SD. Statistical significance was determined using one-way ANOVA with Tukey's post-hoc test (B–E, G) or unpaired two-tailed t-test (F, H). ***$p < 0.001$, **$p < 0.01$, *$p < 0.05$.

DDS alters microglial morphology and enhances phagocytic capacity

Microglial reactivity in AD has been closely linked to morphological alterations associated with tau pathology and Aβ accumulation [39]. We therefore examined whether DDS treatment alters microglial morphology and phagocytic capacity. Our morphological analysis revealed that DDS treatment did not significantly alter the number of Iba1$^+$ reactive microglia, but shifted microglial morphology toward a more homeostatic-like state, characterized by a more ramified appearance with thin, highly branched processes. In contrast, microglia from untreated 3×Tg-AD mice in the hippocampal CA1 region displayed reduced process complexity and diminished arborization, indicative of a persistently activated, non-homeostatic phenotype (**Figure 2A-D**). While similar morphological changes in the DG did not reach statistical significance, microglia in DDS-treated mice exhibited a consistent tendency toward increased process arborization (**Figure S3**). Taken together, these data indicate that DDS primarily remodels microglial phenotype rather than altering

microglial population size.

To further examine the impact of DDS on microglial Aβ phagocytosis, we conducted *in vitro* experiments using BV2 microglial cell. We first evaluated the concentration- and tim e-dependent effects of DDS on microglial viability. DDS at 0, 12.5, 25, 50, 100, and 200 μg/m modestly increased proliferative activity after 24 h of exposure, whereas at 48 h cell viability was significantly reduced only at 200 μg/mL compared with the control group (**Figure S4**). Based on these data, we selected 100 μg/mL DDS for 24 h as the test condition for subsequent *in vitro* assays. We then established an Aβ-induced microglial activation model by exposing BV2 cells to Aβ and found that DDS treatment significantly reduced Aβ levels in Aβ-challenged BV2 microglia (**Figure 2E**). Consistently, DDS treatment significantly enhanced the phagocytosis of pHrodo Red-labeled synaptosomes in both BV2 cells and primary microglia (**Figure 2F, G**). Furthermore, DDS treatment increased microglial uptake of Aβ measured by fluorescent (HiLyte™ Fluor 555)-labeled Aβ peptide (fAβ(1-42)) (**Figure 2H**). Taken together with our *in vivo* observations, these findings indicate that DDS enhances microglial phagocytic capacity toward Aβ and synaptic elements under AD related stress conditions.

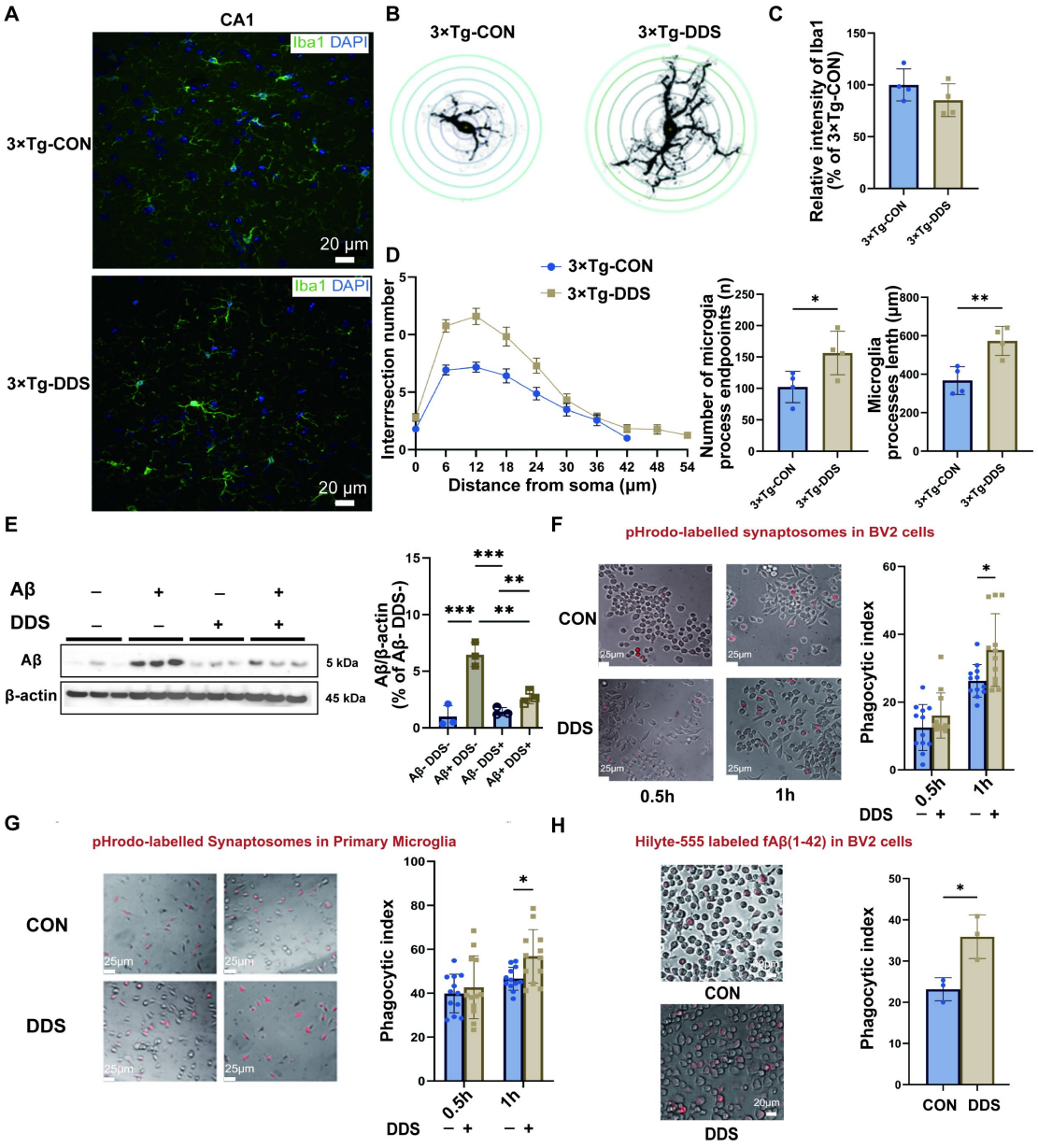

Figure 2. Morphological and functional recovery of microglia following DDS treatment.

(A) Representative immunofluorescence images of the hippocampal CA1 region showing microglia (Iba1, green) and nuclei (DAPI, blue) in 3×Tg-CON and 3×Tg-DDS mice. Scale bar: 20 μm.
(B) Representative two-dimensional Sholl reconstructions of individual CA1 microglia from 3×Tg-CON and 3×Tg-DDS mice.
(C) Quantification of Iba1 fluorescence intensity in CA1 microglia. Four mice per group were analyzed; three fields were quantified per mouse, and values were averaged per mouse for statistical analysis (n = 4).
(D) Sholl-based morphological analysis of CA1 microglia, including the number of intersections as a function of distance from the soma (left), the number of process endpoints per cell (middle), and total process length per cell (right).

Four mice per group were analyzed; values were averaged per mouse for statistical analysis (n = 4).
(E) Western blot analysis of Aβ in BV2 cells, with representative immunoblots from four treatment conditions (Aβ− DDS−, Aβ+ DDS−, Aβ− DDS+, Aβ+ DDS+) and corresponding densitometric quantification normalized to β-actin (n = 3 per group).
(F–G) Synaptic phagocytosis assays in BV2 cells (F) and primary microglia (G) pretreated with or without DDS for 24 h and incubated with pHrodo-labeled synaptosomes for 0.5 h or 1 h (n = 12 per group).
(H) Aβ phagocytosis in BV2 cells treated with fAβ(1-42) ± DDS for 24 h (n = 3 per group).
Data are presented as mean ± SD. Statistical significance was determined using unpaired two-tailed t-test (C, D, F–H) or one-way ANOVA with Tukey's post-hoc test (E). ***$p < 0.001$, **$p < 0.01$, *$p < 0.05$.

Single-cell transcriptomics reveals DDS associated metabolic remodeling and shifts in microglial states

To determine how DDS affects microglial transcriptional programs, we performed single-cell RNA sequencing (scRNA-seq) of hippocampal cells from 3×Tg-AD mice treated with or without DDS for 6 weeks. We obtained 27,465 and 33,266 high-quality transcriptomes from the 3×Tg-DDS and 3×Tg-CON groups, respectively. Cell-type annotation using established marker genes identified the major hippocampal cell types, including microglia, astrocytes, oligodendrocytes, neurons, and vascular cells (**Figure S5A-C**). Although neurons are the most abundant cell type in the central nervous system, only a small number of neurons were captured in our dataset (**Figure S5D**). This pattern is consistent with previous single-cell studies of brain tissue and likely reflects loss of neurons during tissue dissociation. Neurons, with long axons

and complex dendritic arbors, are vulnerable to mechanical stress and enzymatic digestion, particularly during processing at elevated temperature. In contrast, microglia have a more compact morphology and are less vulnerable to these procedures [40, 41]. After quality control, microglia accounted for the largest fraction of captured cells. This enrichment reflects dissociation bias rather than true *in vivo* cell proportions, but it provided sufficient microglial cells for subcluster analysis.

Microglial subcluster proportions were further analyzed based on pathological classification and genotype (**Figure S5E, F**). Guided by differentially expressed genes and previous definitions of homeostatic microglia (HM), disease associated microglia (DAM), microglial neurodegenerative phenotype (MGnD), and cycling/proliferating microglia (CPM), we grouped the microglial clusters into major microglial groups (**Figure 3A, B, Figure S6**). Clusters 0–3 expressed canonical homeostatic markers *P2ry12*, *Cx3cr1*, and *Olfml3* and were designated HM-P2ry12 microglia. Cluster 13, annotated as HM-mt_Nd2, showed higher levels of mitochondrial transcripts, including *mt-Cytb*, *mt-Nd1*, and *mt-Nd2*. This cluster contained few cells and was not used as a main basis for subsequent mechanistic interpretation. Clusters 4,5,8 and 12 exhibited a DAM1-like inflammatory profile (DAM1-Nfkbia) characterized by *Nfkbia*, *Nfkbiz* and *Atf3* upregulation. Cluster6 (DAM1-CPE) represented a putative neuroprotective state co-expressing *Aldoc*, *Clu* and *Cpe*, together with

retained expression of homeostatic microglial markers. Clusters7,10 and11 displayed a canonical DAM/MGnD signature with high *Apoe*, *Clec7a*, *Cst7*, *Lpl*, *Ccl6* and *Spp1* and were classified as DAM2 microglia, whereas cluster9 comprised cycling/proliferating microglia (CPM) marked by *Mki67* and *Top2a*.

Comparative transcriptional profiling between 3×Tg-CON and 3×Tg-DDS microglia identified hundreds of DEGs (**Figure 3C**). DDS treatment preferentially upregulated metabolism related genes and increased expression of the homeostatic marker *P2ry12*, while downregulating the glycolytic enzyme *Hk2*. KEGG enrichment analysis of these DEGs highlighted pathways related to ribosomal function, OXPHOS and glycolysis (**Figure 3D**), suggesting that DDS treatment is associated with changes in microglial energy metabolism and protein synthesis gene programs.

To further define co-expressed transcriptional programs, we performed weighted gene co-expression network analysis (WGCNA) and identified three major modules, including brown, turquoise, and blue modules (**Figure 3E, Figure S7A**). The blue module contained inflammatory and stress-response genes, including *Nfkbia*, *Nfkbiz*, *Atf3*, and *Cd83*, and showed higher expression in DAM1-Nfkbia and DAM2 microglia. This module showed lower expression in 3×Tg-DDS microglia than in 3×Tg-CON microglia (**Figure 3F, Figure S7B**), and pathway enrichment linked it to neuroinflammation and NF-κB signaling (**Figure**

3G). In contrast, the turquoise module was enriched for homeostatic and immune regulatory genes, whereas the brown module was enriched for phagocytosis, ribosome, and proteostasis genes. Both turquoise and brown modules showed higher expression in 3×Tg-DDS microglia. These results suggest that DDS treatment is associated with lower inflammatory related module expression and higher expression of homeostatic, ribosomal, and proteostasis related modules in microglia.

To spatially validate key scRNA-seq–defined transcriptional changes, we performed in situ sequencing analysis of hippocampal microglia. ISS confirmed reduced *PRAS40* and increased *Cpe* transcript abundance in CA1 microglia following DDS treatment, consistent with single-cell transcriptomic results (Figure S8).

DDS treatment is associated with altered microglial communication and state composition in 3×Tg-AD mice

Given the transcriptional and metabolic changes observed in microglia, which may affect intercellular communication, we used CellChat to infer ligand–receptor-mediated signaling among microglial states in 3×Tg-AD mice. Compared with 3×Tg-CON mice, 3×Tg-DDS mice showed a modest increase in overall interaction strength and inter-subtype interaction number (Figure 3H,

Figure S9A). DAM2, DAM1-Nfkbia, DAM1-CPE, CPM, and HM-P2ry12 were the main communication nodes, with strong inter-subtype connections (Figure 3I, Figure S9B). Network diagrams and interaction heatmaps showed increased inferred signaling contribution from DAM1-CPE, HM-P2ry12, and CPM microglia in 3×Tg-DDS mice, whereas interactions involving DAM1-Nfkbia and DAM2 were reduced (Figure S9C, D). These results suggest that DDS treatment is associated with altered predicted communication patterns among microglial states in 3×Tg-AD mice.

Analysis of incoming and outgoing signaling patterns further identified pathway-level differences between microglia from 3×Tg-CON and 3×Tg-DDS mice (Figure 3J, K). In 3×Tg-DDS mice, predicted SEMA4 signaling toward HM-P2ry12 microglia was increased, Galectin and APOE signaling involving DAM1-Nfkbia and DAM1-CPE microglia was enhanced, whereas CADM signaling in DAM1-CPE and DAM2 microglia was reduced. These findings indicate that DDS treatment is associated with predicted ligand receptor signaling among microglial states in 3×Tg-AD mice.

To further examine microglial state transitions, we used Monocle2 to reconstruct pseudotime trajectories of hippocampal microglia (Figure3L, M, Figure S10A, B). The inferred trajectory originated from HM-P2ry12 microglia and showed a branched topology. DAM1-Nfkbia, DAM2, and CPM cells were mainly distributed along one trajectory arm, whereas DAM1-CPE cells were located

along a separate arm. When cells from 3×Tg-CON and 3×Tg-DDS mice were displayed separately in the same pseudotime space and summarized by subcluster composition, 3×Tg-DDS mice showed higher proportions of HM-P2ry12 and DAM1-CPE microglia and a lower proportion of DAM1-Nfkbia associated inflammatory microglia.

We next analyzed pseudotime genes to characterize transcriptional changes during microglial state transitions. A gene module containing *P2ry12*, *Cx3cr1*, *Csf1r*, *Aldoc*, *Cpe*, and *Clu* gradually decreased along pseudotime, indicating reduced HM-P2ry12/DAM1-CPE associated transcriptional features and lower expression of genes related to stress adaptation and proteostasis regulation. In contrast, *Ttr*, *Cd83*, *Atf3*, and *Ccl4* increased along pseudotime, suggesting induction of early activation-, stress-response-, and chemokine related programs. At later pseudotime, *Apoe*, *Il1b*, *Cxcl10*, ribosomal genes, and cell-cycle genes were increased, indicating inflammatory/DAM related activation, increased translational activity, and proliferative programs.

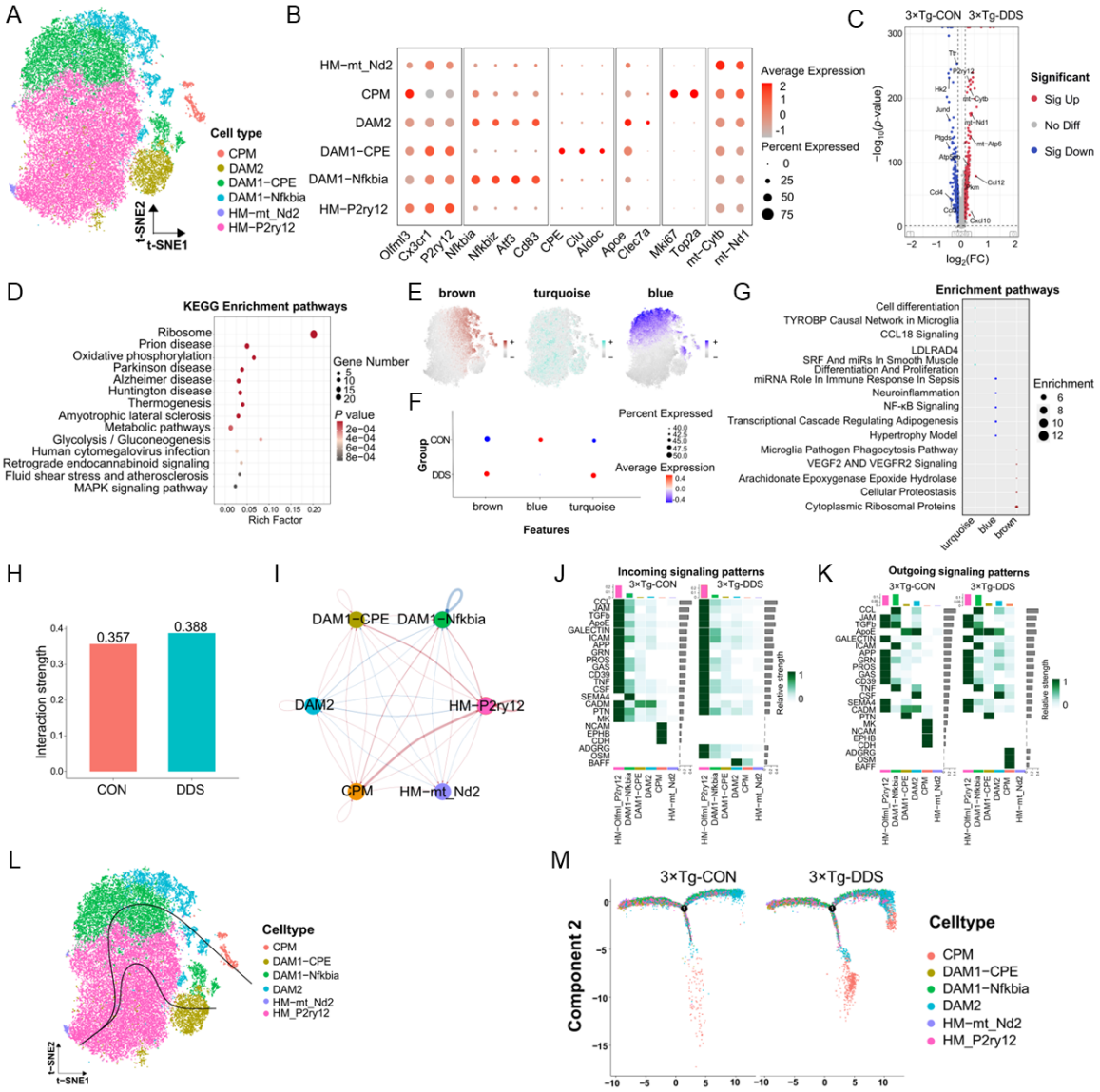

Figure 3. DDS modulates microglial immunometabolic states, intercellular communication, and state transitions in 3×Tg-AD mice.

(A) t-SNE plot resolving transcriptionally distinct microglial populations in the 3×Tg-AD hippocampus, with each cluster delineating a discrete activation state. **(B)** Dot plot displaying canonical marker expression across microglial clusters, where dot size reflects the proportion of expressing cells and color intensity denotes mean expression. **(C)** Volcano plot highlighting differential gene expression between DDS- and vehicle-treated microglia, with significantly upregulated (red) and downregulated (blue) genes meeting adjusted *p*-value ≤ 0.01 and $|\log_2 FC| \geq 0.26$. **(D)** KEGG pathway enrichment of differentially expressed genes, showing the top 14 pathways ranked by $-\log_{10}$ (adjusted *p*-value). **(E–G)** WGCNA identifying three microglial gene co-expression modules (brown, turquoise, blue), comparing module eigengenes between groups, and revealing

WikiPathways enrichment of module genes.
(H–I) CellChat analysis quantifying global ligand–receptor communication strength and visualizing inter-cluster signaling networks among six microglial subpopulations, with edge thickness proportional to signaling intensity.
(J–K) Incoming and outgoing signaling signatures across microglial subclusters, with color intensity indicating the magnitude and DDS-dependent modulation of signal flow.
(L) Pseudotime trajectories capturing microglial state transitions and branchpoint divergence from homeostatic microglia (HM), with trajectory bifurcation reflecting DDS-induced alternative activation routes.
(M) Separate projection of 3×Tg-CON and 3×Tg-DDS microglia onto the shared pseudotime trajectory.

DDS restores microglial mitochondrial function under AD associated conditions

Given the metabolic alterations identified in microglia by scRNA-seq analysis, we next assessed whether DDS treatment restores mitochondrial function under AD associated conditions. To model microglial activation by aggregated Aβ, cells were pre-treated with oligomeric Aβ (oAβ). Mitochondrial analyses showed that DDS altered ROS levels, mitochondrial membrane potential (MMP), and ATP production. In BV2 microglia exposed to oAβ, DDS treatment rescued mitochondrial dysfunction by reducing oAβ-induced ROS overproduction (**Figure 4A, B**), and restoring MMP (**Figure 4C, D**). DDS also increased ATP production in microglia both in the presence and absence of oAβ (**Figure 4E**).

To examine the effects of DDS in primary microglia, we analyzed cells isolated

from 3×Tg-AD mice. Seahorse analysis showed that microglia from 3×Tg-CON mice displayed increased extracellular acidification rates (ECARs, **Figure 4F**) together with reduced oxygen consumption rates (OCRs, **Figure 4J**), indicating a shift to ATP production through glycolysis via metabolic reprogramming [42]. DDS treatment reduced glycolytic capacity and glycolytic reserve (**Figure 4G-4I**). At the same time, DDS treatment increased basal respiration (**Figure 4K**), maximal respiration (**Figure 4L**), and ATP production (**Figure 4M**). These findings indicate that DDS shifts energy production in primary microglia toward mitochondrial respiration.

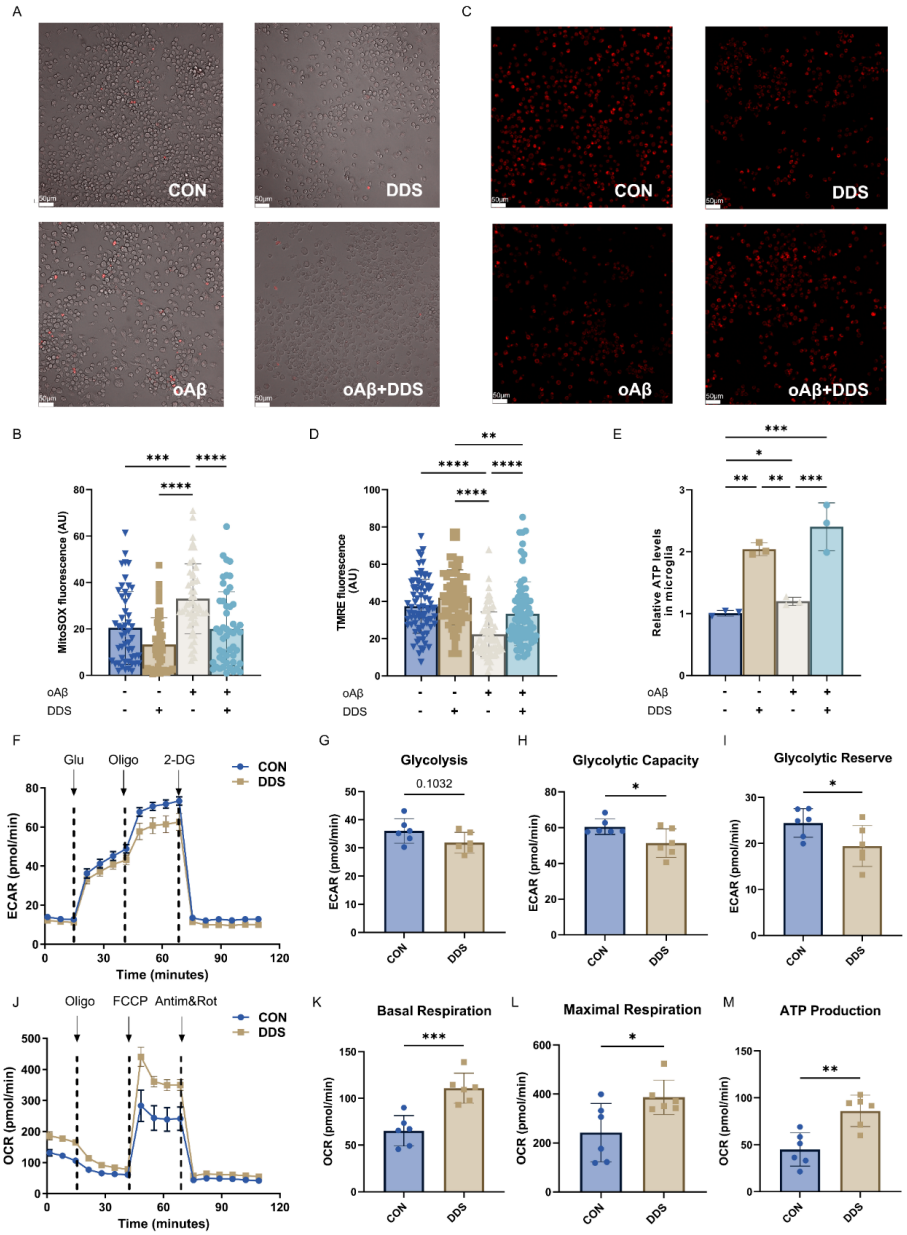

Figure 4. Amelioration of microglial mitochondrial dysfunction in AD pathology through DDS treatment.

(A) Representative MitoSOX fluorescence images of BV2 cells under four treatment conditions (CON, DDS, oAβ, oAβ + DDS). Scale bar: 50 μm.

(B) Quantification of mitochondrial ROS levels assessed by MitoSOX fluorescence. Cells were sampled from three independent wells; n = 50 cells per group.

(C) Representative TMRE fluorescence images of BV2 cells under the same treatment conditions. Scale bar: 50 μm.

(D) Quantification of mitochondrial membrane potential assessed by TMRE fluorescence. Cells were sampled from three independent wells; n = 75 cells per group.

(E) Relative ATP levels in BV2 cells following DDS and oAβ treatment,

normalized to protein content. n = 3 independent experiments per group. **(F–I)** Glycolytic function in primary microglia from 3×Tg-AD mice assessed by ECAR, including time-resolved acidification rates and quantification of basal glycolysis, glycolytic capacity, and glycolytic reserve (n = 6 per group). **(J–M)** Mitochondrial respiratory function measured by OCR in primary microglia, including oxygen consumption traces and quantification of basal respiration, maximal respiration, and spare respiratory capacity (n = 6 per group). Data are presented as mean ± SD. Statistical significance was determined using one-way ANOVA with Tukey's post-hoc test (B, D, E) or unpaired t-test (G–I, K–M). ****$p < 0.0001$, ***$p < 0.001$, **$p < 0.01$, *$p < 0.05$.

DDS interacts with PRAS40 and suppresses mTORC1 signaling

The antimicrobial mechanism of DDS parallels that of sulfonamides, functioning through competitive inhibition of dihydropteroate synthase (DHPS) and subsequent disruption of para-aminobenzoic acid binding, ultimately blocking bacterial folate synthesis [33]. Notably, the absence of DHPS homologs in metazoan cells ensures this mechanism does not affect multicellular organisms. To investigate the molecular mechanism by which DDS enhances cellular metabolism, we employed Drug Affinity Responsive Target Stability (DARTS), an advanced technique that identifies drug-protein interactions by evaluating ligand-induced alterations in protein stability [43]. The excised protein band was subjected to trypsin digestion and identified through nano LC–MS/MS analysis using the MASCOT database (**Figure 5A, Figure S11A-D**). This approach nominated PRAS40 as a candidate DDS-interacting protein.

As an intrinsic inhibitor of mTORC1, PRAS40 directly binds to the complex to exert its inhibitory function. Upon phosphorylation, PRAS40 dissociates from

mTORC1, thereby relieving the inhibitory effect and promoting mTOR activation [44]. PRAS40 and its phosphorylation sites are highly conserved across species [45], while the mTOR signaling pathway similarly exhibits high conservation across diverse species [46, 47]. In hippocampal tissue, western blot analysis showed that DDS significantly reduced the p-PRAS40/PRAS40 ratio, suggesting that DDS affects the phosphorylation state of PRAS40 (**Figure 5B, C**). To investigate potential molecular interactions, docking analysis using a predicted structure of PRAS40 identified a putative binding interface between DDS and PRAS40, wherein the amino groups of DDS interact with residues Ala66, His69, and Pro41 (**Figure 5D, E**). Consistent with these observations, surface plasmon resonance (SPR) measurements supported a measurable DDS–PRAS40 interaction, with an apparent dissociation constant in the mid-micromolar range (KD = 634 μM) (**Figure 5F**).

Given that AKT/mTOR hyperactivation exacerbates Aβ accumulation, impairs autophagy, and drives broad metabolic dysfunction in AD models [48-50], we next interrogated the impact of DDS on this signaling cascade in 3×Tg-AD mice (**Figure 5G, H**). Western blot analysis showed that DDS treatment significantly reduced hippocampal p-AKT (Ser473) levels, with a clear downward trend in the p-AKT/AKT ratio, and significantly increased pGSK3β (Ser9) as well as the pGSK3β/GSK3β ratio, indicative of inhibitory Ser9 phosphorylation of GSK3β. In line with the identification of PRAS40 as a DDS target, DDS significantly

decreased p-mTOR (Ser2448) and the p-mTOR/mTOR ratio, indicating effective suppression of mTORC1 activity *in vivo*.

To further substantiate the modulation of mTOR signaling [51, 52], we examined downstream effectors and autophagy markers (**Figure 5I, J**). DDS significantly reduced phosphorylation of the mTOR effector p70S6K (Thr389) and significantly increased LC3-II levels and the LC3-II/LC3-I ratio, indicating enhanced autophagic activity *in vivo*. DDS significantly decreased the expression of the autophagy substrate p62 (SQSTM1), further confirming the restoration of autophagic flux. Because HIF1α activity is tightly regulated by mTOR signaling and promotes a glycolytic metabolic shift, we next evaluated HIF1α expression and found that DDS significantly reduced hippocampal HIF1α protein levels, suggesting improved microglial metabolic efficiency. In the oAβ-stimulated BV2 microglial cell model, the levels of phosphorylated PRAS40 and mTOR were significantly elevated following oAβ exposure; however, these increases were attenuated by DDS treatment (**Figure S11E-H**). Collectively, these results demonstrate that DDS constrains PRAS40–mTOR signaling activation under both *in vivo* and *in vitro* AD related conditions.

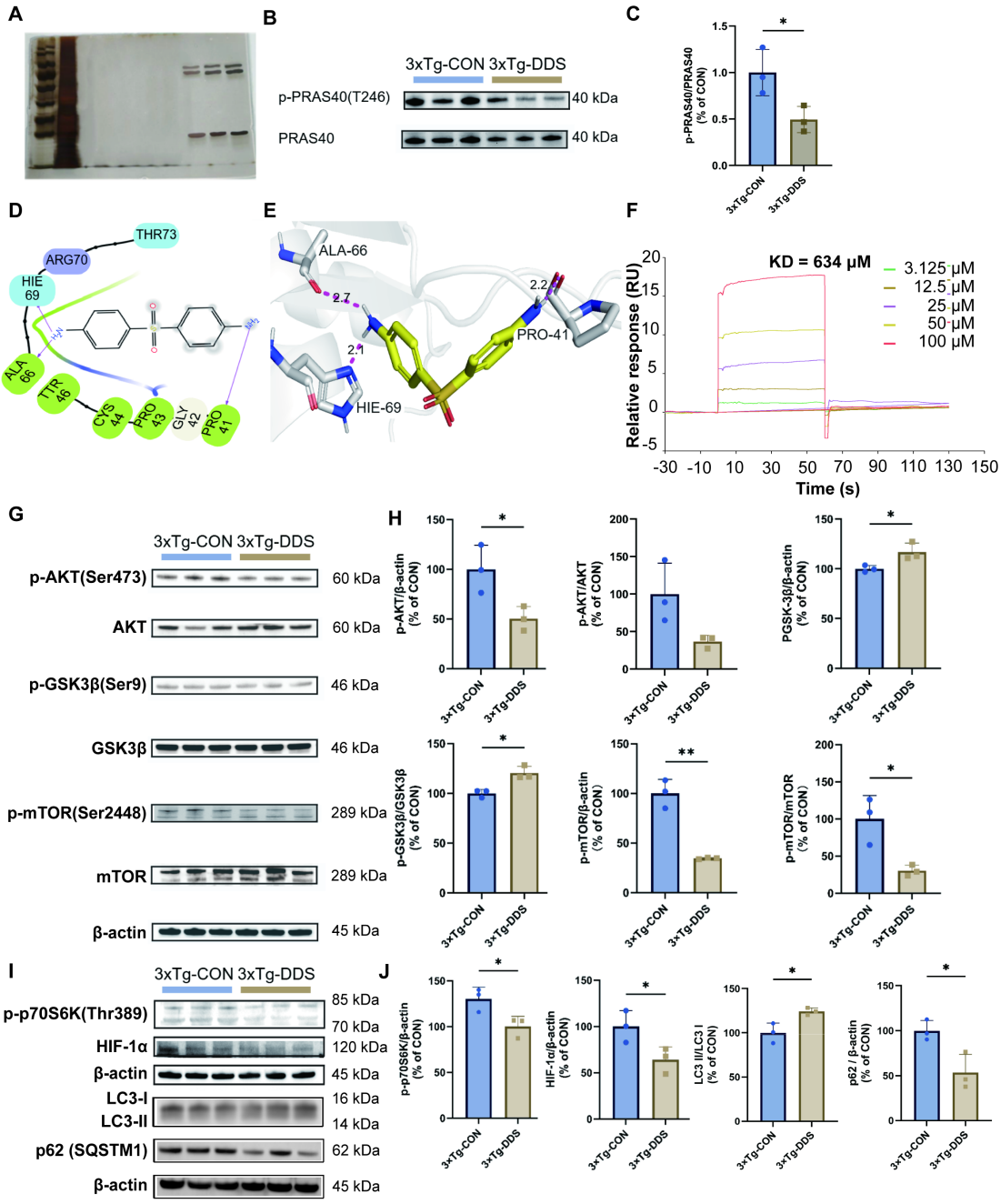

Figure 5. DDS targets PRAS40 and modulates PRAS40-mTORC1 signaling.

(A) DARTS assay with silver staining showing a DDS-protected protein band, which was subsequently identified as PRAS40 by mass spectrometry.
(B–C) Western blot analysis of p-PRAS40 and PRAS40 in hippocampal tissue from 3×Tg-AD mice treated with or without DDS. Quantification shows the p-PRAS40/PRAS40 ratio (n = 3 per group).
(D–E) Structure-based molecular docking models illustrating a predicted DDS–PRAS40 interaction. DDS is shown as yellow sticks, and selected PRAS40 residues are highlighted; docking analysis indicates potential hydrogen-bonding interactions between DDS and PRAS40.

(F) Surface plasmon resonance analysis of DDS–PRAS40 interactions, with representative sensorgrams and steady-state fitting used to estimate apparent binding affinity (KD).
(G–H) Western blot analysis of phosphorylated and total AKT, GSK3β, and mTOR in 3×Tg-AD mice ± DDS treatment (n = 3 per group), normalized to β-actin.
(I–J) Western blot analysis of phosphorylated P70S6K, HIF-1α, LC3-II/I ratio, and p62 (SQSTM1) in 3×Tg-AD mice ± DDS treatment (n = 3 per group), normalized to β-actin.
Graphs show mean ± SD. Statistical significance was determined using unpaired two-tailed t-test. $^{**}p < 0.01$, $^{*}p < 0.05$.

PRAS40–mTOR signaling modulation regulates hippocampal glucose metabolism in 3×Tg-AD mice

Given the importance of brain-wide metabolic flexibility for neuronal homeostasis and its reported disruption in AD pathogenesis [53], we next examined whether PRAS40 mTOR signaling modulation is associated with altered hippocampal glucose metabolism in 3×Tg-AD mice using targeted metabolomic analyses. DDS treatment was associated with normalization of several altered glycolytic and tricarboxylic acid (TCA) cycle intermediates, with metabolite profiles trending toward those observed in C57-CON mice (**Figure 6A**). In untreated 3×Tg-AD mice, glucose-6-phosphate (G6P) and lactate levels were elevated, consistent with accumulation of glycolytic intermediates. DDS treatment reduced the abundance of these metabolites, suggesting attenuation of pathological glycolytic buildup and diversion. In parallel, DDS-treated mice exhibited increased citrate and isocitrate levels together with reduced succinate

and malate, a pattern consistent with enhanced entry of glucose-derived carbon into mitochondrial oxidative pathways. Given the established role of citrate as a negative regulator of phosphofructokinase-1 (PFK-1), these coordinated changes are compatible with a reduction in excessive glycolytic flux and a shift toward more efficient oxidative glucose utilization. Collectively, these findings suggest that DDS does not simply enhance glycolysis, but is associated with improved coordination between glucose uptake, mitochondrial oxidation, and downstream energy metabolism, thereby contributing to partial restoration of metabolic homeostasis in the AD hippocampus.

To further examine these observations in vivo, we performed ^{18}F-fluorodeoxyglucose (FDG) PET imaging (**Figure 6B**). DDS treatment was associated with increased FDG uptake in 3×Tg-AD mice, with higher standardized uptake values (SUVs) observed in both the hippocampus and the whole brain (**Figure 6C, D**). These imaging findings are consistent with the metabolomic profiles and support the notion that DDS treatment is linked to improved cerebral glucose utilization in AD mice.

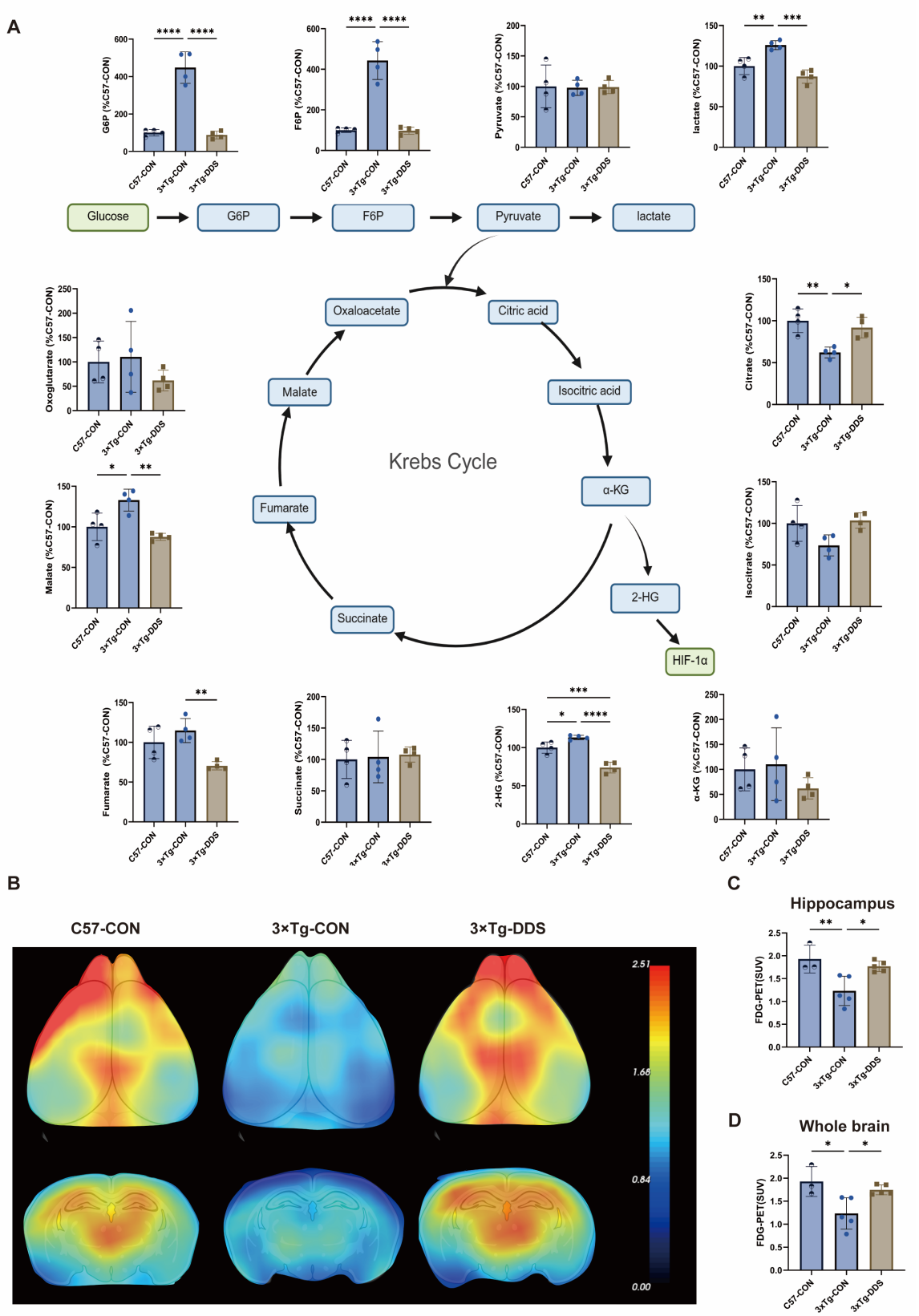

1 **Figure 6. Hippocampal and whole-brain glucose metabolism following**
2 **DDS-mediated PRAS40 modulation.**
3 **(A)** Targeted metabolomic profiling of glycolytic and tricarboxylic acid (TCA)
4 cycle intermediates in hippocampal tissue from C57-CON, 3×Tg-CON, and

3×Tg-DDS mice. Bar plots show relative metabolite levels normalized to C57-CON. The schematic illustrates the glycolytic pathway and TCA cycle, with measured metabolites highlighted. n = 4 per group.
(B) Representative FDG-PET images illustrating cerebral glucose uptake in C57-CON, 3×Tg-CON, and 3×Tg-DDS mice. Axial (top) and coronal (bottom) views are displayed using a standardized uptake value (SUV) scale ranging from 0.00 to 2.51.
(C) Quantification of hippocampal FDG-PET SUV values across the indicated groups (n = 3 for C57-CON; n = 5 for 3×Tg-CON and 3×Tg-DDS).
(D) Quantification of whole-brain FDG-PET SUV values across the same groups.
Data are presented as mean ± SD. Statistical significance was determined using one-way ANOVA with Tukey's post-hoc test. ****$p < 0.0001$, ***$p < 0.001$, **$p < 0.01$, *$p < 0.05$.

Microglia-specific PRAS40 overexpression attenuates DDS associated improvements in AD related pathology in 3×Tg-AD mice

To determine whether the cognitive effects of DDS in 3×Tg-AD mice involve reduced microglial PRAS40 phosphorylation, we overexpressed PRAS40 in microglia using rAAV-PRAS40, with an empty-vector virus (rAAV-C.V.) used as the control (**Figure 7A**). After viral injection and completion of the 6-week treatment period, NOR testing showed that DDS significantly improved recognition memory in the rAAV-C.V.+DDS group compared with the rAAV-C.V.+CON group. This improvement was not observed in rAAV-PRAS40+DDS mice, whose performance was comparable to that of rAAV-PRAS40+CON mice (**Figure 7B**). In the MWM test, DDS increased platform crossings and time spent in the target quadrant in rAAV-C.V. mice, whereas these effects were largely absent after PRAS40 overexpression. Among DDS-treated 3×Tg-AD

mice, PRAS40 overexpression attenuated the spatial memory improvement induced by DDS (**Figure 7C-E**).

Subsequently, we examined hippocampal protein expression (**Figure 7F, G**). DDS reduced PRAS40 protein levels in the rAAV-C.V.+DDS group, whereas rAAV-PRAS40 infection elevated PRAS40 expression and rendered it refractory to DDS-mediated suppression. Consistent with these effects, DDS significantly lowered hippocampal Aβ and tau phosphorylation at the AT8 and AT180 epitopes in the rAAV-C.V.+DDS group. By contrast, PRAS40 overexpression increased baseline Aβ and phospho-tau levels and largely prevented their reduction by DDS, with Aβ, AT8, and AT180 levels in the rAAV-PRAS40+DDS group remaining comparable to those in the rAAV-PRAS40+CON group. Tau-5 levels did not differ among groups, whereas HT7 immunoreactivity was selectively reduced in the rAAV-C.V.+DDS group.

To assess the systemic safety of DDS treatment and rAAV injection, we monitored body weight throughout the 8-week experimental period and evaluated hepatic and renal function at the study endpoint (**Figure S12A-D**). Body weight remained stable throughout the experimental period, with no group-dependent differences. Liver and kidney weights were comparable across groups. Serum markers of hepatic function, including alanine aminotransferase (ALT), aspartate aminotransferase (AST), and alkaline phosphatase (ALP), as well as the renal function marker creatinine, showed no

significant differences among groups. Histological examination of liver and kidney sections showed no overt necrosis, inflammation, or fibrosis in any group.

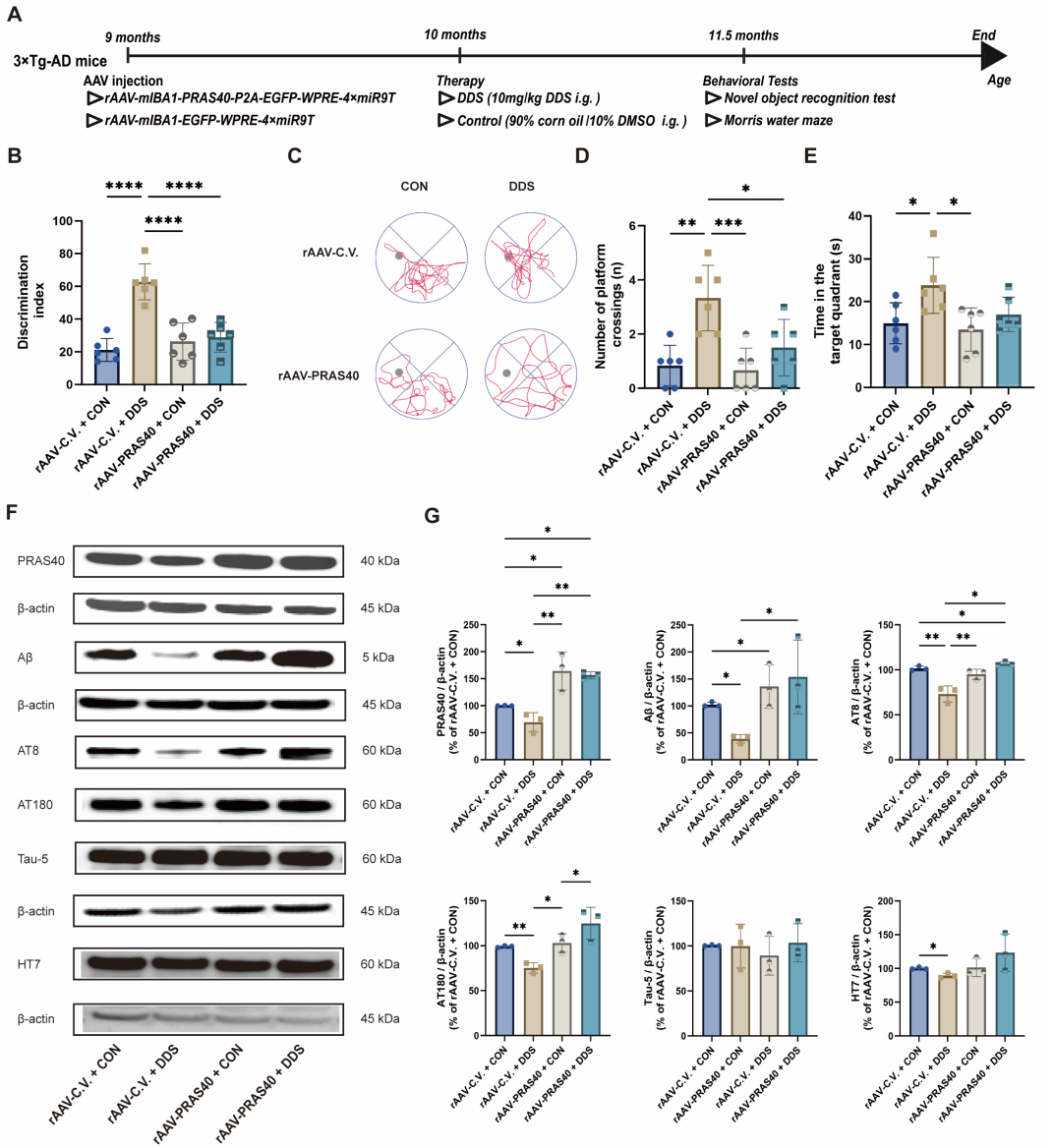

Figure 7. Targeted microglial PRAS40 overexpression attenuates DDS associated therapeutic benefits in 3×Tg-AD mice.

(A) Experimental timeline for AAV injection, DDS administration, and behavioral testing in 3×Tg-AD mice, with four groups defined by AAV vector and treatment: rAAV-C.V.+CON, rAAV-C.V.+DDS, rAAV-PRAS40+CON, and rAAV-PRAS40+DDS (n = 6 per group).

(B) Discrimination index in the novel object recognition test showing loss of DDS-mediated cognitive improvement upon PRAS40 overexpression.

(C–E) Morris water maze performance, including representative swimming paths during the probe test (C), number of platform crossings (D), and time spent in the target quadrant (E).

(F–G) Western blot analysis of hippocampal PRAS40 and AD related proteins, with representative immunoblots of PRAS40, Aβ, phospho-tau (AT8, AT180), and total tau (Tau-5, HT7) (F) and densitometric quantification normalized to β-actin (G; n = 3 per group).
Data are presented as mean ± SD. Statistical significance was determined using one-way ANOVA with Tukey's post-hoc test. ***$p < 0.001$, **$p < 0.01$, *$p < 0.05$.

Microglia-specific PRAS40 knockdown rescues AD related pathology and supports pharmacological targeting

To determine whether reducing microglial PRAS40 is sufficient to improve AD related phenotypes, we knocked down PRAS40 in 3×Tg-AD mice using rAAV-shPRAS40, with rAAV-shC.V. serving as a scramble control (**Figure 8A**). PRAS40 knockdown produced marked cognitive improvements in the NOR test, the rAAV-shPRAS40 group exhibited a significantly higher discrimination index than controls (**Figure 8B**). In the MWM testing, PRAS40 knockdown increased platform crossings and shortened the latency to first entry, whereas time spent in the target quadrant did not differ significantly between groups (**Figure 8C-F**).

Protein analyses confirmed that rAAV-mediated PRAS40 knockdown was effectively achieved at the tissue level and was accompanied by reduced hippocampal Aβ levels and decreased tau phosphorylation at the AT8 epitope, while total tau (HT7) remained unchanged (**Figure 8G, H**). These findings indicate that microglial PRAS40 knockdown is sufficient to improve cognitive deficits and reduce key pathological features in 3×Tg-AD mice. Safety assessment showed no significant differences in serum ALT, AST, ALP, or

CREA levels between the rAAV-shPRAS40 and rAAV-shC.V. groups (**Figure S12E**). HE-stained liver and kidney sections showed no overt histological abnormalities in either group (**Figure S12F**).

To identify small-molecule inhibitors targeting PRAS40, we performed an in silico virtual screen using the SPECS small-molecule database (https://www.specs.net/), which yielded 15 candidate compounds predicted to bind PRAS40 (**Figure S13A, table S1**). Structure-based molecular docking, together with SPR assays, supported measurable interactions between recombinant PRAS40 and several candidate compounds, with Compound F1 (KD = 1.35 μM) and Compound F2 (KD = 79.9 μM) exhibiting the strongest apparent affinities (**Figure S13B-E, table S2**). In BV2 microglia exposed to oAβ, compounds F1-F4 increased synaptosome uptake, partially alleviating the oAβimpairment of microglial phagocytic function (**Figure S13F, G**). Collectively, microglia-specific PRAS40 knockdown improved behavioral performance and reduced pathological features in AD mice. In parallel, several PRAS40-binding

compounds enhanced phagocytic activity in oAβ-treated microglia.

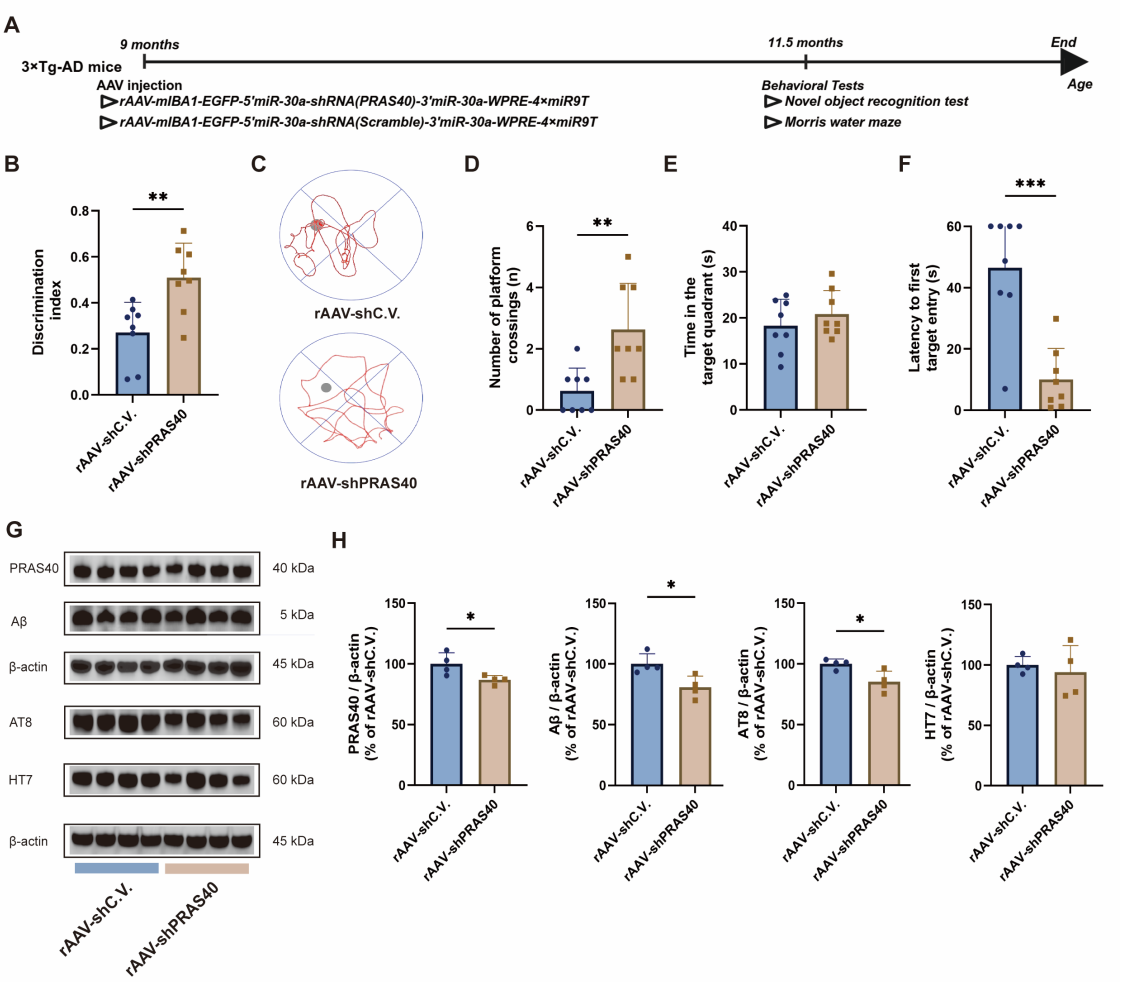

Figure 8. Targeted microglial PRAS40 knockdown ameliorates cognitive deficits and pathology in 3×Tg-AD mice.

(A) Experimental timeline for rAAV injection and behavioral testing in 3×Tg-AD mice, with two groups defined by AAV vector: rAAV-shC.V. (scramble control) and rAAV-shPRAS40 (n = 8 per group), the latter achieving microglial PRAS40 knockdown.

(B–F) Behavioral performance, including discrimination index in the NOR test (B), representative swimming paths during the probe test (C), number of platform crossings in the probe trial (D), time spent in the target quadrant (E), and latency to first entry (F).

(G–H) Western blot analysis of hippocampal PRAS40 and AD related proteins, with representative immunoblots of PRAS40, Aβ, phospho-tau (AT8), and total tau (HT7) and densitometric quantification normalized to β-actin (n = 4 per group).

Data are presented as mean ± SD. Statistical significance was determined using an unpaired two-tailed t-test. ***$p < 0.001$, **$p < 0.01$, *$p < 0.05$.

Discussion

AD is characterized by chronic neuroinflammation, metabolic dysfunction, and impaired handling of Aβ and tau pathology. In this study, DDS improved cognitive performance and reduced neuropathological changes in 3×Tg-AD mice (**Figure 9**). These effects were accompanied by reduced PRAS40 phosphorylation, lower mTORC1 downstream signaling, enhanced autophagy, microglial metabolic reprogramming, and changes in microglial transcriptional states. Consistently, metabolomic analysis and FDG-PET imaging showed that DDS was associated with improved hippocampal energy metabolism in 3×Tg-AD mice. These findings support microglial PRAS40–mTORC1 signaling as a pathway involved in microglial metabolic reprogramming and AD pathological and metabolic changes.

Our scRNA-seq analysis suggests that DDS does not simply suppress microglial activation, but is associated with changes in microglial state composition in 3×Tg-AD mice. The increase in HM-P2ry12 microglia and DAM1-CPE microglia, together with the reduction in DAM1-Nfkbia associated inflammatory microglia, may indicate a more adaptive microglial response in AD. Rather than reflecting generalized microglial activation, this pattern suggests retention of homeostatic and proteostasis features while limiting NF-κB-linked inflammatory signaling, which may help restrain chronic neuroinflammation and AD related proteotoxic stress. The increase in DAM1-

CPE microglia is also notable because this subtype was characterized by *Aldoc*, *Clu*, and *Cpe* expression together with retained homeostatic microglial markers. Previous studies have suggested that CPE may contribute to the regulation of tau phosphorylation, Aβ burden, synaptic integrity, and microglial homeostasis in AD models [54-56]. Thus, the DDS associated increase in DAM1-CPE microglia may reflect a DAM1 related state that retains homeostatic markers and shows metabolic and protein-handling features, rather than a broad suppression of microglial activation.

Microglial phagocytic and inflammatory functions are closely linked to cellular metabolic state [57]. In AD, microglia shift from OXPHOS to glycolysis, leading to reduced ATP availability, impaired clearance of pathological aggregates, and increased oxidative stress [58-62]. In our study, DDS increased mitochondrial respiration and ATP production, reduced ROS levels, and improved mitochondrial membrane potential in microglia exposed to oAβ. These findings suggest that DDS promotes microglial metabolic reprogramming toward a more energy-efficient state, which may support phagocytic activity and limit inflammatory stress. Metabolomic analysis and FDG-PET imaging further showed changes in hippocampal glucose metabolism, suggesting that DDS associated improvement in microglial metabolism was accompanied by broader improvements in energy metabolism in the AD hippocampus.

An important finding of this study is the identification of PRAS40 as a key

mediator of DDS associated microglial metabolic reprogramming. PRAS40 acts upstream of mTORC1, a central regulator of autophagy and metabolic flux that is dysregulated in AD [52, 63-65], and may contribute to the restoration of microglial function after DDS treatment. *In vivo,* microglia-specific PRAS40 overexpression attenuated the cognitive and pathological benefits of DDS, whereas PRAS40 knockdown alone recapitulated key behavioral and pathological features observed with DDS treatment. In addition, compounds predicted to bind PRAS40 partially recapitulated DDS-induced enhancement of microglial phagocytosis. Together, these findings suggest that PRAS40 contributes to the regulation of microglial metabolism and function in response to DDS treatment. Targeting microglial PRAS40–mTORC1 signaling to restore microglial metabolic homeostasis may provide a potential strategy for improving AD pathological and functional deficits.

From a translational perspective, drug repurposing may help accelerate the development of AD treatments by reducing the time and cost required for de novo drug development [66, 67]. Repurposed agents currently represent nearly one-third of the AD drug development pipeline, reflecting growing interest in this approach [68]. DDS, a medication with decades of clinical use and well-established pharmacokinetic and safety profiles, is therefore an attractive repurposing candidate. Although dapsone hypersensitivity syndrome affects a small subset of patients (1.0–1.4%) [69, 70], this risk can be minimized through

HLA-B*13:01 screening [25, 70, 71]. Consistent with its known clinical profile, our study confirmed excellent tolerability of DDS in microglial cultures and in 3×Tg-AD mice, with no evidence of hepatic or renal toxicity. Importantly, compared with current high-cost AD therapies with limited accessibility [72, 73], DDS offers a low-cost, widely accessible option with clear translational potential.

Several limitations should be noted. First, although the 3×Tg-AD mouse model captures key pathological features of AD, it does not fully reflect the molecular and cellular complexity of human AD. In addition, our analyses were performed in male mice. Previous studies in AD mouse models have reported sex differences in metabolism and disease progression, suggesting that the present findings may not fully apply to female mice. Future studies using female mice and additional AD models will be needed to determine whether the effects of DDS are also present across different sex and model backgrounds. Second, the scRNA-seq dataset was affected by cell-type bias during tissue dissociation, as described in the Results. This bias allowed detailed analysis of microglial transcriptional states but limits our ability to determine all brain cell types affected by DDS. However, our focus on microglia is supported not only by the scRNA-seq results but also by immunostaining validation, *in vitro* microglial functional assays, and *in vivo* microglial PRAS40 overexpression and knockdown. Thus, the current evidence most strongly supports a role for DDS in microglia. Future studies using methods less affected by dissociation bias,

along with targeted validation in specific brain cell types, will be needed to determine whether DDS also affects neurons or other cells in the AD brain. Third, although our experiments support an important role for PRAS40 in DDS action, DDS may also act through other pathways that were not examined in this study. Future proteomic analysis after chronic DDS treatment, combined with PRAS40-targeted validation, may help identify PRAS40-dependent and PRAS40-independent effects. Finally, our results identify PRAS40 as a potential therapeutic target that requires further validation in more human-relevant models. Several PRAS40-binding compounds partially reproduced the effects of DDS *in vitro*, and their efficacy, specificity, and safety need to be tested *in vivo*. Artificial intelligence-based screening and computational drug discovery may help identify and optimize PRAS40-targeted compounds [74, 75]. Together with experimental validation, this approach may support the development of more potent and selective PRAS40-directed therapies for AD.

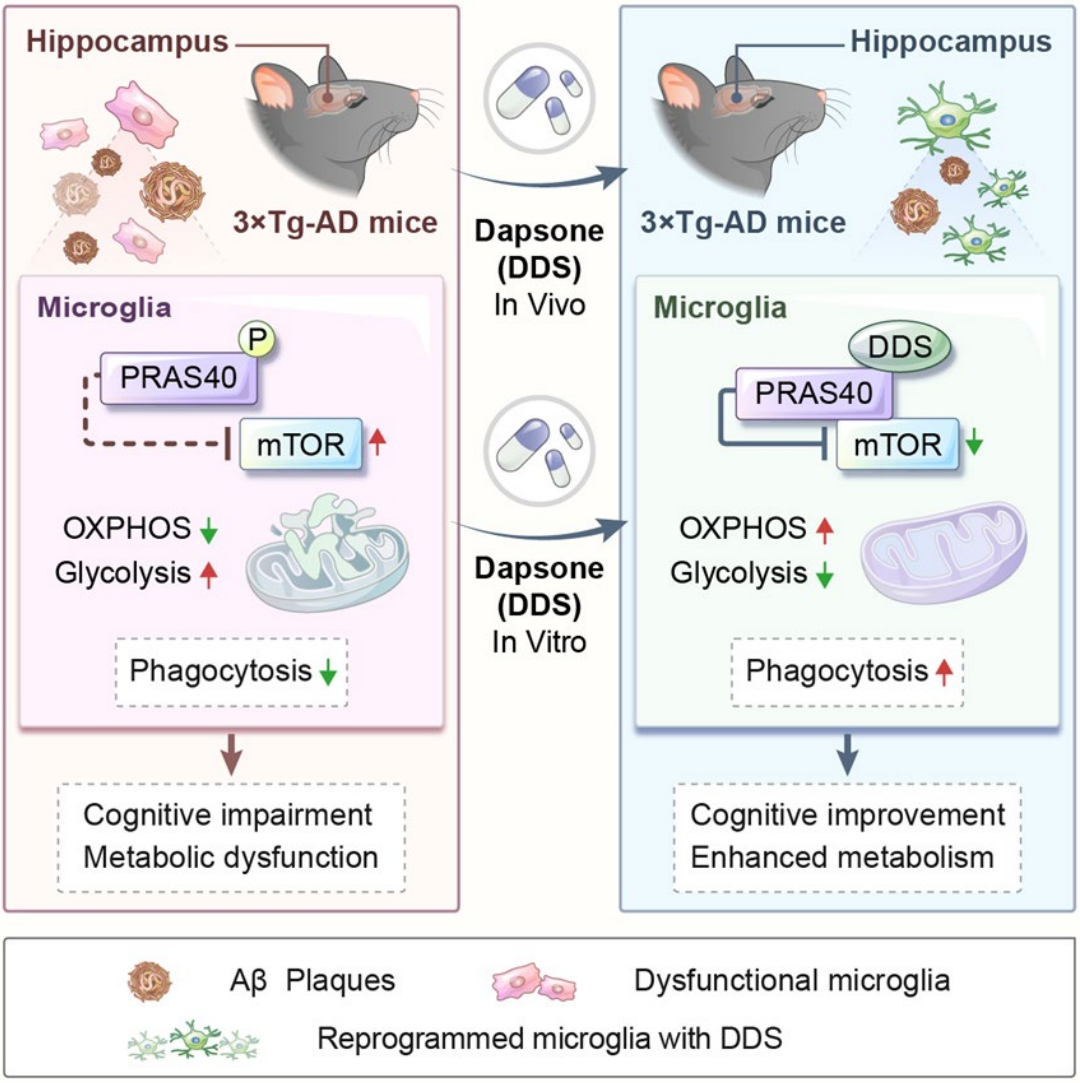

Figure 9. PRAS40-mTORC1-dependent microglial regulation by DDS ameliorates AD pathology

Schematic summary of DDS-mediated regulation of microglial immunometabolism in 3×Tg-AD mice. In the AD state, increased PRAS40 activity and mTOR signaling in microglia are associated with a metabolic shift toward glycolysis, impaired mitochondrial oxidative phosphorylation, reduced phagocytic capacity, and progressive hippocampal Aβ accumulation, contributing to metabolic dysfunction and cognitive impairment. DDS treatment attenuates PRAS40 mTOR signaling in microglia, promotes a shift toward oxidative phosphorylation, restores mitochondrial and autophagic function, and enhances phagocytosis, thereby reducing pathological burden and improving cognitive performance in 3×Tg-AD mice.

Conclusion

DDS reduced AD pathology in 3×Tg-AD mice and improved microglial function under oAβ-challenged conditions, accompanied by reduced microglial PRAS40–mTORC1 signaling, changes in microglial states, and improved metabolic and autophagy function. These findings support microglial PRAS40–mTORC1 signaling as a pathway involved in the effects of DDS and suggest that targeting this pathway to regulate microglial metabolism may provide a potential therapeutic strategy for AD.

1 List of abbreviations

Abbreviation	Full term
3×Tg-AD	Triple-transgenic Alzheimer's disease mouse model
AAV	Adeno associated viral
AD	Alzheimer's disease
ALP	Alkaline phosphatase
ALT	Alanine aminotransferase
AST	Aspartate aminotransferase
Aβ	Amyloid-β
CCK-8	Cell Counting Kit-8
CPM	Cycling/proliferating microglia
DAM	Disease associated microglia
DARTS	Drug Affinity Responsive Target Stability
DDS	Dapsone
DEGs	Differentially expressed genes
DG	Dentate gyrus
DHPS	Dihyperteroate synthase
ECAR	Extracellular acidification rate
fAβ	fluorescent -labeled Aβ peptide
FBS	Fetal bovine serum
fEPSP	Field excitatory postsynaptic potential
G6P	Glucose-6-phosphate
HM	Homeostatic microglia
HTVS	High-throughput virtual screening
ISS	In situ sequencing
LTP	Long-term potentiation
MMP	Mitochondrial membrane potential
mTORC1	Mechanistic target of rapamycin complex 1
MWM	Morris water maze
NOR	Novel object recognition
OCR	Oxygen consumption rate
OXPHOS	Oxidative phosphorylation
PFK-1	Phosphofructokinase-1
PRAS40	Proline-rich Akt substrate of 40 kDa
ROI	Region of interest
ROS	Reactive oxygen species

scRNA-seq	Single-cell RNA sequencing
shRNA	Short hairpin RNA
SP	Standard precision
SUV	Standardized uptake value
TCA	Tricarboxylic acid
TMRE	Tetramethylrhodamine ethyl ester
WGCNA	Weighted Gene Co-expression Network Analysis

1

Author information

Feng SF and Qiu NZ have contributed equally to this work.

Contributions

Lu L and Yuan K contributed to conceptualization, project administration, supervision, and writing – review and editing. Lu L also contributed to funding acquisition and resources. Feng SF contributed to data curation, formal analysis, investigation, methodology, validation, writing – original draft, and writing – review and editing. Qiu NZ, Han L, Cao L, and Lu TS contributed to data curation, formal analysis, investigation, methodology, and validation. Lu TS also contributed to visualization and writing – review and editing. Zihang Li, Liu SY, and Guo LY contributed to investigation. Meng SQ and Huang CX contributed to visualization and writing – review and editing. Shi J, Wei YB, Furen Zhang, Yin QQ, and Liu XX contributed to writing – review and editing. All authors reviewed and approved the final version of the manuscript.

Corresponding authors

Correspondence to Yin QQ, Furen Zhang, Wei Y B, Yuan K and Lu L.

Ethics declarations

Ethics approval and consent to participate

All animal procedures complied with relevant ethical regulations for animal research and were approved by the Institutional Animal Care and Use Committee of Peking University.

Consent for publication

Not applicable.

Competing interests

The authors declare that they have no conflicts of interest (financial or otherwise) related to the data presented in this manuscript.

Availability of data and materials

All data needed to evaluate the conclusions in the paper are present in the paper and/or the Supplementary Materials. Additional data related to this paper may be requested from the authors.

Funding

This work was supported in part by the National Programs for Brain Science and Brain-like Intelligence Technology of China (STI2030-Major Projects, 2021ZD0200800), the National Natural Science Foundation of China (no. 82288101, no. 82371499), the Fundamental Research Funds for the Central Universities (Peking University Medicine Fund for world's leading discipline or discipline cluster development, BMU2022DJXK007).

Acknowledgments

We are grateful for bioinformatics support from Yonghong Dong and Bailin Duan (LC-BioTechnology co.,ltd.).

References

1. Ostrowitzki S, Bittner T, Sink KM, Mackey H, Rabe C, Honig LS, Cassetta E, Woodward M, Boada M, van Dyck CH, et al: **Evaluating the Safety and Efficacy of Crenezumab vs Placebo in Adults With Early Alzheimer Disease: Two Phase 3 Randomized Placebo-Controlled Trials.** *JAMA Neurol* 2022, **79:**1113-1121.
2. Cummings J, Zhou Y, Lee G, Zhong K, Fonseca J, Cheng F: **Alzheimer's disease drug development pipeline: 2024.** *Alzheimers Dement (N Y)* 2024, **10:**e12465.
3. Wicker A, Shriram J, Decourt B, Sabbagh MN: **Passive Anti-amyloid Beta Monoclonal Antibodies: Lessons Learned over Past 20 Years.** *Neurol Ther* 2024, **13:**1571-1595.
4. Lozupone M, Dibello V, Sardone R, Castellana F, Zupo R, Lampignano L, Bortone I, Stallone R, Altamura M, Bellomo A, et al: **Lessons learned from the failure of solanezumab as a prospective treatment strategy for Alzheimer's disease.** *Expert Opin Drug Discov* 2024, **19:**639-647.
5. Cummings JL, Cohen S, van Dyck CH, Brody M, Curtis C, Cho W, Ward M, Friesenhahn M, Rabe C, Brunstein F, et al: **ABBY: A phase 2 randomized trial of crenezumab in mild to moderate Alzheimer disease.** *Neurology* 2018, **90:**e1889-e1897.
6. Budd Haeberlein S, Aisen PS, Barkhof F, Chalkias S, Chen T, Cohen S, Dent G, Hansson O, Harrison K, von Hehn C, et al: **Two Randomized Phase 3 Studies of Aducanumab in Early Alzheimer's Disease.** *J Prev Alzheimers Dis* 2022, **9:**197-210.
7. van Dyck CH, Swanson CJ, Aisen P, Bateman RJ, Chen C, Gee M, Kanekiyo M, Li D, Reyderman L, Cohen S, et al: **Lecanemab in Early Alzheimer's Disease.** *N Engl J Med* 2023, **388:**9-21.
8. Prillaman M: **Heralded Alzheimer's drug works - but safety concerns loom.** *Nature* 2022, **612:**197-198.
9. Thambisetty M, Howard R: **Lecanemab trial in AD brings hope but requires greater clarity.** *Nat Rev Neurol* 2023, **19:**132-133.
10. Spangenberg EE, Green KN: **Inflammation in Alzheimer's disease: Lessons learned from microglia-de pletion models.** *Brain, behavior, and immunity*, **61:**1-11.
11. Salter MW, Stevens B: **Microglia emerge as central players in brain disease.** *Nat Med* 2017, **23:**1018-1027.
12. Zhan Y, Paolicelli RC, Sforazzini F, Weinhard L, Bolasco G, Pagani F, Vyssotski AL, Bifone A, Gozzi A, Ragozzino D: **Deficient neuron-microglia signaling results in impaired functional brain connectivity and social behavior.** *Nature neuroscience* 2014, **17:**400-406.
13. Monje ML, Toda H, Palmer TD: **Inflammatory Blockade Restores**

Adult Hippocampal Neurogenesis. *Science* 2003, **302:**1760-1765.

14. Frigerio CS, Wolfs L, Fattorelli N, Thrupp N, Voytyuk I, Schmidt I, Mancuso R, Chen W-T, Woodbury ME, Srivastava G: **The major risk factors for Alzheimer's disease: age, sex, and genes modulate the microglia response to Aβ plaques.** *Cell reports* 2019, **27:**1293-1306. e1296.
15. McIntosh A, Mela V, Harty C, Minogue AM, Costello DA, Kerskens C, Lynch MA: **Iron accumulation in microglia triggers a cascade of events that leads to altered metabolism and compromised function in APP/PS1 mice.** *Brain Pathology* 2019, **29:**606-621.
16. Fang EF, Hou Y, Palikaras K, Adriaanse BA, Kerr JS, Yang B, Lautrup S, Hasan-Olive MM, Caponio D, Dan X: **Mitophagy inhibits amyloid-β and tau pathology and reverses cognitive deficits in models of Alzheimer's disease.** *Nat Neurosci* 2019, **22:**401-412.
17. Lepiarz-Raba I, Gbadamosi I, Florea R, Paolicelli RC, Jawaid A: **Metabolic regulation of microglial phagocytosis: Implications for Alzheimer's disease therapeutics.** *Transl Neurodegener* 2023, **12:**48.
18. Leng L, Yuan Z, Pan R, Su X, Wang H, Xue J, Zhuang K, Gao J, Chen Z, Lin H: **Microglial hexokinase 2 deficiency increases ATP generation through lipid metabolism leading to β-amyloid clearance.** *Nature Metabolism* 2022, **4:**1287-1305.
19. Rim C, You M-J, Nahm M, Kwon M-S: **Emerging role of senescent microglia in brain aging-related neurodegenerative diseases.** *Translational Neurodegeneration* 2024, **13:**10.
20. Baik SH, Kang S, Lee W, Choi H, Chung S, Kim J-I, Mook-Jung I: **A Breakdown in Metabolic Reprogramming Causes Microglia Dysfunction in Alzheimer's Disease.** *Cell Metabolism* 2019, **30:**493-507.e496.
21. Fromm E, Wittmann J: **Derivate des p-Nitrothiophenols.** *Berichte der deutschen chemischen Gesellschaft* 1908, **41:**2264-2273.
22. Wozel VG: **Innovative use of dapsone.** *Dermatologic clinics* 2010, **28:**599-610.
23. Ahmad RA, Rogers HJ: **Pharmacokinetics and protein binding interactions of dapsone and pyrimethamine.** *Br J Clin Pharmacol* 1980, **10:**519-524.
24. Zhang FR, Liu H, Irwanto A, Fu XA, Li Y, Yu GQ, Yu YX, Chen MF, Low HQ, Li JH, et al: **HLA-B*13:01 and the dapsone hypersensitivity syndrome.** *New England Journal of Medicine* 2013, **369:**1620-1628.
25. Liu H, Wang Z, Bao F, Wang C, Sun L, Zhang H, Yu G, Mi Z, Li J, Li L, et al: **Evaluation of Prospective HLA-B*13:01 Screening to Prevent Dapsone Hypersensitivity Syndrome in Patients With Leprosy.** *JAMA Dermatology* 2019, **155:**666-672.

26. MCGEER PL, KLEGERIS A, WALKER DG, YASUHARA O, MCGEER EG: **Pathological proteins in senile plaques.** *The Tohoku journal of experimental medicine* 1994, **174:**269-277.
27. Kanwar BA, Khattak A, Balentine J, Lee JH, Kast RE: **Benefits of Using Dapsone in Patients Hospitalized with COVID-19.** *Vaccines (Basel)* 2022, **10**.
28. Goto M, Kimura T, Hagio S, Ueda K, Kitajima S-i, Tokunaga H, Sato E: **Neuropathological analysis of dementia in a Japanese leprosarium.** *Dementia and Geriatric Cognitive Disorders* 1995, **6:**157-161.
29. Lee JH, Kanwar B, Lee CJ, Sergi C, Coleman MD: **Dapsone is an anticatalysis for Alzheimer's disease exacerbation.** *iScience* 2022, **25:**104274.
30. Oddo S, Caccamo A, Kitazawa M, Tseng BP, LaFerla FM: **Amyloid deposition precedes tangle formation in a triple transgenic model of Alzheimer's disease.** *Neurobiol Aging* 2003, **24:**1063-1070.
31. Oddo S, Caccamo A, Shepherd JD, Murphy MP, Golde TE, Kayed R, Metherate R, Mattson MP, Akbari Y, LaFerla FM: **Triple-transgenic model of Alzheimer's disease with plaques and tangles: intracellular Aβ and synaptic dysfunction.** *Neuron* 2003, **39:**409-421.
32. Zhan R, Zhao M, Zhou T, Chen Y, Yu W, Zhao L, Zhang T, Wang H, Yang H, Jin Y, et al: **Dapsone protects brain microvascular integrity from high-fat diet induced LDL oxidation.** *Cell Death Dis* 2018, **9:**683.
33. Coleman MD: **Dapsone: modes of action, toxicity and possible strategies for increasing patient tolerance.** *Br J Dermatol* 1993, **129:**507-513.
34. d'Isa R, Comi G, Leocani L: **Apparatus design and behavioural testing protocol for the evaluation of spatial working memory in mice through the spontaneous alternation T-maze.** *Sci Rep* 2021, **11:**21177.
35. Bromley-Brits K, Deng Y, Song W: **Morris water maze test for learning and memory deficits in Alzheimer's disease model mice.** *J Vis Exp* 2011.
36. Codocedo JF, Mera-Reina C, Bor-Chian Lin P, Fallen PB, Puntambekar SS, Casali BT, Jury-Garfe N, Martinez P, Lasagna-Reeves CA, Landreth GE: **Therapeutic targeting of immunometabolism reveals a critical reliance on hexokinase 2 dosage for microglial activation and Alzheimer's progression.** *Cell Rep* 2024, **43**.
37. Xiong W, Xu K, Sun JK, Liu S, Zhao B, Shi J, Herrup K, Chow HM, Lu L, Li J: **The mitochondrial long non-coding RNA lncMtloop regulates mitochondrial transcription and suppresses Alzheimer's disease.** *Embo j* 2024, **43:**6001-6031.
38. Jiang Z, Liu B, Lu T, Liu X, Lv R, Yuan K, Zhu M, Wang X, Li S, Xu S, et

al: **SGK1 drives hippocampal demyelination and diabetes-associated cognitive dysfunction in mice.** *Nat Commun* 2025, **16:**1709.

39. Dani M, Wood M, Mizoguchi R, Fan Z, Walker Z, Morgan R, Hinz R, Biju M, Kuruvilla T, Brooks DJ, Edison P: **Microglial activation correlates in vivo with both tau and amyloid in Alzheimer's disease.** *Brain* 2018, **141:**2740-2754.
40. Mattei D, Ivanov A, van Oostrum M, Pantelyushin S, Richetto J, Mueller F, Beffinger M, Schellhammer L, Vom Berg J, Wollscheid B, et al: **Enzymatic Dissociation Induces Transcriptional and Proteotype Bias in Brain Cell Populations.** *International Journal of Molecular Sciences* 2020, **21**.
41. Jo KW, Lee D, Cha DG, Oh E, Choi YH, Kim S, Park ES, Kim JK, Kim KT: **Gossypetin ameliorates 5xFAD spatial learning and memory through enhanced phagocytosis against Aβ.** *Alzheimer's Research & Therapy* 2022, **14:**158.
42. Yao J, Irwin RW, Zhao L, Nilsen J, Hamilton RT, Brinton RD: **Mitochondrial bioenergetic deficit precedes Alzheimer's pathology in female mouse model of Alzheimer's disease.** *Proc Natl Acad Sci U S A* 2009, **106:**14670-14675.
43. Lomenick B, Hao R, Jonai N, Chin RM, Aghajan M, Warburton S, Wang J, Wu RP, Gomez F, Loo JA: **Target identification using drug affinity responsive target stability (DARTS).** *Proc Natl Acad Sci U S A* 2009, **106:**21984-21989.
44. Yang H, Jiang X, Li B, Yang HJ, Miller M, Yang A, Dhar A, Pavletich NP: **Mechanisms of mTORC1 activation by RHEB and inhibition by PRAS40.** *Nature* 2017, **552:**368-373.
45. Nascimento EB, Ouwens DM: **PRAS40: target or modulator of mTORC1 signalling and insulin action?** *Arch Physiol Biochem* 2009, **115:**163-175.
46. Zoncu R, Efeyan A, Sabatini DM: **mTOR: from growth signal integration to cancer, diabetes and ageing.** *Nature Reviews Molecular Cell Biology* 2011, **12:**21-35.
47. Liu GY, Sabatini DM: **mTOR at the nexus of nutrition, growth, ageing and disease.** *Nat Rev Mol Cell Biol* 2020, **21:**183-203.
48. Yang W, Yang LF, Song ZQ, Shah SZA, Cui YY, Li CS, Zhao HF, Gao HL, Zhou XM, Zhao DM: **PRAS40 alleviates neurotoxic prion peptide-induced apoptosis via mTOR-AKT signaling.** *CNS Neuroscience & Therapeutics* 2017, **23:**416-427.
49. Cai S, Yang Q, Cao Y, Li Y, Liu J, Wang J, Zhang X, Liu L, Li X, Zhang Y: **PF4 antagonizes retinal neovascularization via inhibiting PRAS40 phosphorylation in a mouse model of oxygen-induced**

retinopathy. *Biochimica et Biophysica Acta (BBA) - Molecular Basis of Disease* 2020, **1866:**165604.

50. Bernier L-P, York EM, Kamyabi A, Choi HB, Weilinger NL, MacVicar BA: **Microglial metabolic flexibility supports immune surveillance of the brain parenchyma.** *Nature Communications* 2020, **11:**1559.

51. Díaz-Troya S, Pérez-Pérez ME, Florencio FJ, Crespo JL: **The role of TOR in autophagy regulation from yeast to plants and mammals.** *Autophagy* 2008, **4:**851-865.

52. Caccamo A, Majumder S, Richardson A, Strong R, Oddo S: **Molecular interplay between mammalian target of rapamycin (mTOR), amyloid-beta, and Tau: effects on cognitive impairments.** *J Biol Chem* 2010, **285:**13107-13120.

53. Tang BL: **Glucose, glycolysis, and neurodegenerative diseases.** *J Cell Physiol* 2020, **235:**7653-7662.

54. Xiao L, Sharma VK, Toulabi L, Yang X, Lee C, Abebe D, Peltekian A, Arnaoutova I, Lou H, Loh YP: **Neurotrophic factor-α1, a novel tropin is critical for the prevention of stress-induced hippocampal CA3 cell death and cognitive dysfunction in mice: comparison to BDNF.** *Transl Psychiatry* 2021, **11:**24.

55. Xiao L, Yang X, Sharma VK, Abebe D, Loh YP: **Hippocampal delivery of neurotrophic factor-α1/carboxypeptidase E gene prevents neurodegeneration, amyloidosis, memory loss in Alzheimer's Disease male mice.** *Mol Psychiatry* 2023, **28:**3332-3342.

56. Fan FC, Liu LM, Guo M, Du Y, Chen YW, Loh YP, Cheng Y: **Neurotrophic factor-α1/carboxypeptidase E controls progression and reversal of Alzheimer's disease pathogenesis in mice.** *Theranostics* 2025, **15:**2279-2292.

57. Lewcock JW, Schlepckow K, Di Paolo G, Tahirovic S, Monroe KM, Haass C: **Emerging Microglia Biology Defines Novel Therapeutic Approaches for Alzheimer's Disease.** *Neuron* 2020, **108:**801-821.

58. Khosravi M, Peter J, Wintering NA, Serruya M, Shamchi SP, Werner TJ, Alavi A, Newberg AB: **18F-FDG Is a Superior Indicator of Cognitive Performance Compared to 18F-Florbetapir in Alzheimer's Disease and Mild Cognitive Impairment Evaluation: A Global Quantitative Analysis.** *J Alzheimers Dis* 2019, **70:**1197-1207.

59. Cho S, Lee H, Seo J: **Impact of genetic risk factors for Alzheimer's disease on brain glucose metabolism.** *Molecular Neurobiology* 2021, **58:**2608-2619.

60. Ma X, Zhang Y, Gou D, Ma J, Du J, Wang C, Li S, Cui H: **Metabolic reprogramming of microglia enhances proinflammatory cytokine release through EphA2/p38 MAPK pathway in Alzheimer's disease.** *Journal of Alzheimer's Disease* 2022, **88:**771-785.

61. Pan RY, Ma J, Kong XX, Wang XF, Li SS, Qi XL, Yan YH, Cheng J, Liu Q, Jin W, et al: **Sodium rutin ameliorates Alzheimer's disease-like pathology by enhancing microglial amyloid-β clearance.** *Sci Adv* 2019, **5:**eaau6328.
62. Sangineto M, Ciarnelli M, Cassano T, Radesco A, Moola A, Bukke VN, Romano A, Villani R, Kanwal H, Capitanio N, et al: **Metabolic reprogramming in inflammatory microglia indicates a potential way of targeting inflammation in Alzheimer's disease.** *Redox Biol* 2023, **66:**102846.
63. Caccamo A, Maldonado MA, Majumder S, Medina DX, Holbein W, Magrí A, Oddo S: **Naturally secreted amyloid-beta increases mammalian target of rapamycin (mTOR) activity via a PRAS40-mediated mechanism.** *J Biol Chem* 2011, **286:**8924-8932.
64. Lafay-Chebassier C, Paccalin M, Page G, Barc-Pain S, Perault-Pochat MC, Gil R, Pradier L, Hugon J: **mTOR/p70S6k signalling alteration by Abeta exposure as well as in APP-PS1 transgenic models and in patients with Alzheimer's disease.** *J Neurochem* 2005, **94:**215-225.
65. An WL, Cowburn RF, Li L, Braak H, Alafuzoff I, Iqbal K, Iqbal IG, Winblad B, Pei JJ: **Up-regulation of phosphorylated/activated p70 S6 kinase and its relationship to neurofibrillary pathology in Alzheimer's disease.** *The American Journal of Pathology* 2003, **163:**591-607.
66. Cummings J, Zhou Y, Lee G, Zhong K, Fonseca J, Cheng F: **Alzheimer's disease drug development pipeline: 2023.** *Alzheimers Dement (N Y)* 2023, **9:**e12385.
67. Bauzon J, Lee G, Cummings J: **Repurposed agents in the Alzheimer's disease drug development pipeline.** *Alzheimers Res Ther* 2020, **12:**98.
68. Parvathaneni V, Kulkarni NS, Muth A, Gupta V: **Drug repurposing: a promising tool to accelerate the drug discovery process.** *Drug Discov Today* 2019, **24:**2076-2085.
69. Lorenz M, Wozel G, Schmitt J: **Hypersensitivity reactions to dapsone: a systematic review.** *Acta Derm Venereol* 2012, **92:**194-199.
70. Tian W, Shen J, Zhou M, Yan L, Zhang G: **Dapsone hypersensitivity syndrome among leprosy patients in China.** *Lepr Rev* 2012, **83:**370-377.
71. Krismawati H, Irwanto A, Pongtiku A, Irwan ID, Maladan Y, Sitanggang YA, Wahyuni T, Tanjung R, Sun Y, Liu H, et al: **Validation study of HLA-B*13:01 as a biomarker of dapsone hypersensitivity syndrome in leprosy patients in Indonesia.** *PLOS Neglected Tropical Diseases* 2020, **14:**e0008746.
72. **2024 Alzheimer's disease facts and figures.** *Alzheimers Dement* 2024, **20:**3708-3821.

73. **Global, regional, and national burden of Alzheimer's disease and other dementias, 1990-2016: a systematic analysis for the Global Burden of Disease Study 2016.** *Lancet Neurol* 2019, **18:**88-106.

74. Costa F, Gomez Doblas JJ, Díaz Expósito A, Adamo M, D'Ascenzo F, Kołtowski L, Saba L, Mendieta G, Gragnano F, Calabrò P, et al: **Artificial intelligence in cardiovascular pharmacotherapy: applications and perspectives.** *Eur Heart J* 2025, **46:**3616-3627.

75. Bordukova M, Makarov N, Rodriguez-Esteban R, Schmich F, Menden MP: **Generative artificial intelligence empowers digital twins in drug discovery and clinical trials.** *Expert Opin Drug Discov* 2024, **19:**33-42.